

Controlling instabilities in tokamak plasmas through modeling and experiments



UNIVERSITÀ
degli STUDI
di CATANIA

Concetta Barcellona

Supervisor: Prof. Luigi Fortuna

Advisor: Dr. Arturo Buscarino

Dr. Basilio Esposito

Department of Electrical, Electronics and Computer
Engineering
Università degli Studi di Catania

*Doctor of Philosophy in Ingegneria dei Sistemi, Energetica,
Informatica e delle Telecomunicazioni*
October 2020

"If we knew what it was we were doing, it would not be called research, would it?"

Albert Einstein

Acknowledgements

It's already been three years since I started my PhD path. I have lived intense years, full of studies, feelings, discoveries. I have accumulated a wealth of experiences and memories that I will carry forever with me. My path was made special by so many wonderful people that I had the good fortune to know.

Firstly, I would like to express my deepest thanks to my supervisor Professor Luigi Fortuna for guiding me throughout these three years of my academic life. My passion for chaotic systems and research activities has been inspired by his amazing lessons, often enriched with life lessons.

I would like to thank my advisor Dr. Arturo Buscarino for helping me during my PhD course with his teaching and suggestions.

I also would like to thank my advisor Dr. Basilio Esposito for his guidance and expertise. Since the first PhD year, I had the opportunity to collaborate with the research group of the Enea centre of Frascati. This chance allowed me to get passionate to the world of the nuclear fusion, trying to give my contribution to make the nuclear fusion process self-sustainable. A special thank goes to Giorgio Ghillardi for being a supportive and collaborative colleague during

the last year of my PhD, thank you for all the explanations and productive works done together.

During my second PhD year, I was a visitor student at the Universitat Politècnica de Catalunya, where I worked under the supervision of Professor Cristina Masoller. I would like to express my gratitude to the professor for taking me in the DONLL (dynamics, nonlinear optics and lasers) group, full of expert and clever collaborators. A special thanks goes to all the colleagues that worked with me: Donatus, Jordi and Pablo, and all the others colleagues of the group.

The thesis work of the last year was done in remote collaboration with the Plasma Theory research group of Chalmers University of Technology, working under the supervision of Professor Tünde Fülöp. I would like to thank professor for her availability and for giving me the possibility to collaborate with her competent group. I also would like to thank Mathias Hoppe for all the support, explanations and availability.

I would like to thank Professor Maide Bucolo and Eng. Carlo Famoso for their valuable advices and sharing of knowledge.

A special acknowledgement goes to all the colleagues of my laboratory for all the time spending working together: Claudia, Dario G., Emanuela, Dario M., Giuseppe S., Giovanna, Emanuele, Loubna, Donato, Luciano, Domenico, Giuseppe A., Valentina and all the people that I met in the laboratory during these years and my PhD colleagues. Sometime the colleagues became friends as happened to us in our "Caotici group", that I thank. A special thank goes also to signor Felice, for the pleasant break talking together with us.

My gratitude also extends to all my friends, housemates and amazing people meet at the Contamination Lab.

A special thank goes to the Andrea's family, Flavia, Mario, Sonia and nonna Rosetta, for their love and constant presence.

I thank my aunt Graziella for her wisdom and for sharing her knowledge with me. I would like to thank also my uncle Vito and all my cousins.

A deeply thank goes to my parents, who sustained and encouraged me for all my life.

I am very grateful to Michela, my sister friend, for always be present in my life.

A special thank goes to Andrea, who always supports me. Without him, I would not be here today writing these lines. I dedicate this result to him.

Concetta

Abstract

The dream of obtaining a green source of energy, reproducing the fusion process occurring in nature inside the stars, has been pursued for many years by the scientific community. Although significant results have been achieved, unstable phenomena are one of the main concerns in future fusion plasma reactors, such as ITER, that is the largest experimental tokamak under construction.

Edge localized modes and runaway electrons are two of the most relevant problems in tokamak dynamics.

The aim of this thesis is to design and test new techniques to identify and control instabilities affecting plasma performance. Different approaches have been investigated, ranging from practical experiments using electrical analogue to synchrotron images processing and simulations.

The first part of the thesis focuses on the design of an electrical analogue of the plasma behavioural model, exploiting a qualitative low dimensional model of plasma instabilities. The central part of the thesis regards runaway electrons detection and simulations. An automatic platform for the runaway electron pitch angle estimation is implemented. Progressively, the synchrotron images are analysed us-

ing a diagnostic simulation, based on a simplified theoretical model. In the last part of the work, a comparative study of remote recovery algorithms of audio signal paves the way for new applications in the nuclear fusion diagnostics field.

Generally, results confirm the theoretical hypothesis and experimental data, giving a contribution in the path to make the nuclear fusion process self-sustainable.

Keywords: nonlinear systems, nuclear fusion, tokamak, diagnostic, signal processing

Contents

List of acronyms	xv
List of Figures	xvii
List of Tables	xxi
1 Introduction	1
1.1 Motivation	1
1.2 Nuclear Fusion	2
1.2.1 Fusion energy	2
1.2.2 Tokamak	3
1.2.3 Electron dynamics	4
1.2.4 Plasma instabilities	6
1.2.5 FTU	7
1.3 Thesis outline	9
2 Nonlinear circuits to model and control plasma instabilities	15
2.1 Introduction	15
2.2 Plasma lower dimensional model	17
2.2.1 The dynamical model	18

2.2.2	Circuit implementation	18
2.2.3	Dynamical regions and behaviour	22
2.3	Pellet injection	25
2.3.1	The dynamical model	27
2.3.2	Circuit implementation	28
2.3.3	Results	29
2.4	Thermostat control	32
2.4.1	The dynamical model	32
2.4.2	Circuit implementation	33
2.4.3	Results	35
2.5	The Jerk dynamics	35
2.5.1	The Jerk Form of plasma instabilities model	36
2.5.2	Circuit implementation	39
2.6	Conclusion	41
3	Image-Processing for the Estimation of Pitch Angle for Run-	
	away Electrons in Tokamak	45
3.1	Introduction	45
3.2	Runaway Electrons	46
3.3	Synchrotron radiation	47
3.4	Detection system	49
3.5	RE characterisation	51
3.6	Architecture of the software platform	54
3.7	Simulation results	56
3.8	Conclusion	60
4	Simulation of Runaway Electrons synchrotron radiation in	
	FTU	63

4.1	Introduction	63
4.2	Preliminary studies	64
4.2.1	Data selection	64
4.2.2	Time setting images port 3	65
4.2.3	Intensity light variation	67
4.2.4	Plasma parameters	69
4.3	SOFT parameters selection	71
4.3.1	Radiation diagnostic	71
4.3.2	Detector	73
4.3.3	Magnetic field	75
4.3.4	Distribution function	78
4.3.5	Phase space grid	81
4.4	Radial profile of runaway electrons	83
4.4.1	Radial distribution	83
4.4.2	Image inversion procedure	84
4.5	Results	86
4.6	Conclusion	88
5	Remote recovery of audio signals from videos of optical speckle patterns	89
5.1	Introduction	89
5.2	Experimental setup	90
5.3	Recovery methods and performance measures	91
5.3.1	Methods	91
5.3.2	Differential processing scheme (DIF)	92
5.3.3	Mean intensity (MI)	92
5.3.4	1-pixel method (1 PIX)	93
5.3.5	Cross-Correlation (CC)	93

5.3.6	Machine learning method (ML)	95
5.3.7	MIT method	96
5.3.8	Performance measures	96
5.4	Results	97
5.5	Conclusion	99
6	Overall Conclusions and Future Perspectives	101
	Bibliography	105

List of acronyms

Acronyms / Abbreviations

ELMs Edge Localized Modes

FFT Fast Fourier Transform

FTU Frascati Tokamak Upgrade

PCB Printed Circuit Board

PFC Plasma Facing Components

REIS Runaway Electron Imaging and Spectroscopy System

RE Runaway Electrons

SINAD Signal to Noise and Distortion ratio

SOFT Synchrotron-detecting Orbit Following Toolkit

List of Figures

1.2	Particle orbit in a magnetic field	5
1.3	Frascati Tokamak Upgrade (FTU)	7
2.1	Circuit diagram	21
2.2	Physical implementation of the circuit	22
2.3	Damped oscillations $(\delta, \eta) = (0.5, 0.668)$	23
2.4	Periodic oscillations $(\delta, \eta) = (0.5, 0.55)$	24
2.5	Chaotic oscillations $(\delta, \eta) = (0.5, 0.08)$	24
2.6	ELMs oscillations $(\delta, \eta) = (0.5, 0.011)$	25
2.7	Analysis of the dynamical behaviour of the system 2.1 with respect to the parameter η	26
2.8	Circuit diagram in the case of pellet injection.	28
2.9	Experimental trend of z variable before pellet injection.	29
2.10	Experimental trend of ELMs during pellet injection ($\eta =$ 0.5 and $t_{period} = 50$). Perturbations P(t) are shown by green lines in the case (a) and by red lines in the case (b).	30
2.11	Experimental trend of the attractor on the zy-plane before pellet injection.	31

2.12	Experimental trend of the attractor on the zy -plane after pellet injection.	31
2.13	Experimental trend of ELMs with pellet injection by varying the parameter t_{period} . Perturbations $P(t)$ are shown by green lines in the case (a) and by red lines in the case (b).	32
2.14	Circuit diagram in the case of thermostat control.	34
2.15	Attractors in the case of thermostat control application.	35
2.16	Bifurcation diagrams with respect to the control parameter k	36
2.17	Attractors of plasma model in jerk form	39
2.18	Circuit diagram of the plasma model in jerk form.	41
2.19	Jerk plasma lower dimensional model circuit.	42
3.1	Example of FTU visible light image	48
3.2	Overview of the Detection system	49
3.3	Overview of the REIS head	50
3.4	Synchrotron emission spectra at different energies and different pitch angle parameters	51
3.5	Schematic of the extension of the detected synchrotron radiation in the horizontal direction.	53
3.6	Time sequence of RE visible light images	54
3.7	Flow chart of the MATLAB platform.	55
3.8	First steps of the image-processing algorithm.	57
3.9	Zoom on the spot of the RE.	58
3.10	Second part of the image-processing algorithm.	59
3.11	Axes of the fitted ellipse.	60

3.12 Graph of the pitch angle trend for different FTU discharges.	61
4.2 Original FTU image	66
4.3 Experimental synchrotron spectra at $700ms$	66
4.4 Selected image area.	68
4.5 Light intensity variation analysis.	68
4.6 Ratio pixels images variation/ fw spectrometer variation.	69
4.7 Plasma parameters time traces for shot #43651	70
4.8 Coordinate system convention.	73
4.9 Shox: toroidal magnetic field B_0 . It can be, approximately, considered constant in the range of interest $0 - 0.9s$	76
4.10 Shox: safety factor.	77
4.11 Loop voltage and density time traces in the case of shot #43651.	79
4.12 Plasma effective charge Z_{eff} time trace for shot #43651.	80
4.13 Pitch angle variation analysis.	82
4.14 Gaussian radial profile.	83
4.15 Comparison of synchrotron images using different radial profile distribution.	84
4.16 Output results of the image inversion procedure.	85
4.17 Radial profile fitting.	85
4.18 Best spectra results at $700ms$	87
4.19 Best images results at $700ms$	87
5.1 Experimental setup & Example of a speckle image	90
5.2 Performance measures	97

5.3 Methods performance comparison 98

List of Tables

1.1	Main FTU parameters.	8
4.1	Main important parameters of pulse #43651 at time 0.25s.	65
5.1	Performance of the song recovery for three volume lev- els and mean execution time.	98

Chapter 1

Introduction

1.1 Motivation

Nowadays, a defining issue for the planet and humanity is *climate change*. It has been proved scientifically [1] that, with the 95 percent certainty, the dominant cause of global warming is human activity since the mid-20th century. The effects are particularly clear: ocean and atmosphere warming, melting of the glaciers, sea level rise and increasing amounts of greenhouse gases. The role of greenhouse gas emissions in the climate system changing is predominant. One of the primary source of greenhouse gases is carbon dioxide (CO_2), coming from burning fossil fuels. For these reasons, to counter this treat it is necessary to replace natural gas, oil and coal with green source of energy.

In this perspective, an innovative and promising technique to obtain clean energy is *nuclear fusion* [2]. This alternative source could

guarantee the generation of unlimited, carbon-free, clean and safe energy for the future.

1.2 Nuclear Fusion

One of the main challenges in the field of energy production is the fulfilment of the nuclear fusion process.

1.2.1 Fusion energy

Nuclear fusion is a physical process in which two or more atomic nuclei from separate lighter atoms (generally the hydrogen isotopes: deuterium and tritium) are fused together obtaining a nucleus of a heavier atom. The difference in mass between the products of the reaction and the reactants themselves is freed as large amount of energy, the *fusion energy* [3], in accordance with the Einstein's mass-energy equivalence $E = mc^2$, where c is the speed of light in vacuum. The fusion process occurs in nature inside the stars like the sun, where at very high temperature any gas becomes plasma, known as the fourth state of the matter. The plasma is an ionised gas, in which the electrons are completely separated from the ions and it's globally neutral [4]. To reproduce the same process in a laboratory, three conditions must be satisfied: extreme temperature (in order of 150 million °C), high plasma particle density so that collisions may happen and a specific confinement time [5]. In particular, in plasma state the positively charged atomic nuclei are completely separated from the negative charged atomic nuclei. In order to reproduce the same process that takes place in nature, the colliding particle

requires high temperatures, much more higher than the sun, to overcome the repulsive force acting between them. The extremely high temperatures entail a specific device for the plasma confinement, in order to guarantee a self-sustained fusion reactions. Different reactors, with different confinement configurations, are under study [6]. One of the main fusion devices used to contain and control plasma for large-scale fusion production is currently the *tokamak*, a Russian acronym used to indicate a torus-shaped chamber with magnetic coils. Presently, the largest experimental tokamak aiming at the demonstration of fusion as viable energy source (ITER) is under construction at Cadarache, France. It is a worldwide collaboration between USA, Russian Federation, India, China, Europe, Korea and Japan [7].

1.2.2 Tokamak

The tokamak is a thermonuclear fusion device, designed by Soviet scientists in 1950 [8]. This reactor consists in a toroidal chamber, that confines plasma using magnetic fields. It is known also as vacuum chamber, because the inner side must be maintained continually in a vacuum state by a pumping system.

The plasma configuration can be guaranteed only for a limited period of time, but it is necessary to confine plasma long enough for fusion reaction to occur. The plasma is kept in a safe position by strong magnetic fields, in order to maintain it far away from plasma facing components (PFC).

To achieve a stable plasma equilibrium, the magnetic field lines are generated by a combination of toroidal magnetic field (travelling

around the torus) and poloidal magnetic field (travelling in circles orthogonal to the toroidal field) [4], as shown in Figure 1.1.

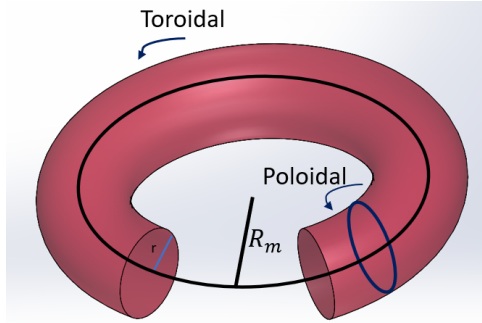


Figure 1.1 Schematic representation of a tokamak coordinate system.

The large amount of current flowing along the toroidal direction of the device is an essential component in the tokamak configuration and a main feature among the magnetic confinement devices. In particular, the magnetic field in the poloidal direction generated by the current opposes the plasma particle drift motion that would otherwise bring them out of the device.

1.2.3 Electron dynamics

In presence of magnetic field, charged particles describe an helical trajectory, approximately around the magnetic field line, as shown in Figure 1.2. The dynamic of the single electron is governed by the Lorentz force:

$$\mathbf{F} = -e(\mathbf{E} + \mathbf{v} \times \mathbf{B}) \quad (1.1)$$

where e is the elementary charge with velocity v , E and B are the electric and magnetic field respectively. The motion of the particle can be decomposed in two components: rapid gyro motion that is perpendicular to the magnetic field and guiding-center motion, approximately along the magnetic field (indicated in the Figure 1.2).

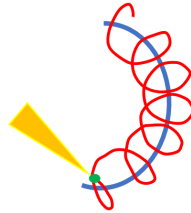


Figure 1.2 Particle orbit in a magnetic field. The picture shows the gyro motion (in red) and the guiding-center motion (blue). The synchrotron radiation emission cone is indicated in yellow (it will better discussed in Chapter 3).

The equations of motion can be solved for each particle by using Eq. (1.1), in order to investigate the dynamics of electrons inside the plasma. However, the particle density inside a tokamak is in the order of $\sim 10^{20} m^{-3}$, so this method is huge from a computational point of view. Another technique that can be followed to investigate the electrons dynamics is a statistical method, a probability distribution is propagated in time in order to localise an electron. The probability distribution is known as *distribution function* and it is, generally indicated as $f(\mathbf{x}, \mathbf{p}, t)$. Usually it is normalised and the integration over all the phase spaces coordinates gives the total number of electrons.

1.2.4 Plasma instabilities

So far, a self-sustained fusion reaction has not been reached. Complex phenomena emerge during different type of instabilities in plasma, affecting the overall plasma performance.

One of the most threatening unstable phenomena is the *edge localized modes* (ELMs) [9], that may lead to severe damages to the vessel components. ELMs are repetitive bursts occurring in the plasma edge. Due to their periodicity, this disruptive instability can be thought as an ELMs cycle. ELMs can damage wall components (especially divertor plates or limiter materials) or can potentially couple or trigger other instabilities. On the basis of the ELMs type and plasma device, ELMs could remove plasma energy and particles. The investigation of the behaviour of the plasma and the occurrence of ELMs by means of a qualitative model can be very useful to mimic the behaviour of physical experiments and test the control strategies to apply.

In certain circumstance, instabilities can cause the dissipation of the toroidal current and the plasma cooling [10], [11]. In this condition, named plasma disruption, a strong electric field, can accelerate electrons to velocities close to the speed of light, giving rise to the phenomenon of *runaway electrons* (RE). In plasma, the friction force acting in collisions with other particles decreases when increasing the velocity of the particles. In particular, electrons have a lighter mass, so they can be accelerated easily to elevated energies [12]. RE are one of the main concerns in tokamak plasma since they are lost in the first wall, causing local melting, local energy deposition and damage on the PFC. Therefore, one of the main challenges in future

fusion devices is the RE detection and control. Imaging techniques can be a powerful tool for the detection of RE when they are still confined within the plasma and to infer the main parameters.

The aim of this thesis is to design and test new techniques to identify and control unstable phenomena affecting plasma stability. Part of the work of this thesis is based on experimental tokamak data collected in the Frascati Tokamak Upgrade.

1.2.5 FTU

The *Frascati Tokamak Upgrade* (FTU), shown in Figure 1.3, is a medium size tokamak machine that has operated in the period 1990 – 2019 at ENEA Frascati, in Italy.

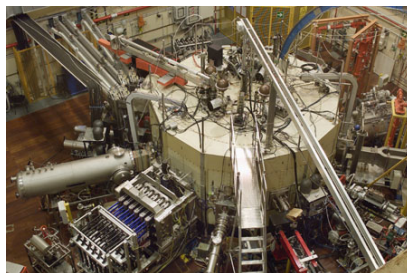


Figure 1.3 Frascati Tokamak Upgrade (FTU) top view [13].

Table 1.1 summarises the main characteristics of the FTU machine. The mechanical structure is composed by a monolithic toroidal magnet that supports the windings and the vacuum chamber. The windings are copper coils; their resistivity must to be decreased at the level of the liquid nitrogen operating temperature (about -196°C) in order to decrease the dissipation due to the Joule effect and consequently

FTU parameters	Value	SI base unit
Plasma major radius (R_m)	0.935	m
Plasma minor radius (r_{minor})	0.31	m
Maximum Plasma Current	1.6	MA
Toroidal Magnetic Field (B_0)	8	T
Toroidal Field flat-top duration	1.5	s
Load Assembly weight	~90	t
Toroidal Field Energy	160	MJ
Poloidal Field Energy	200	MJ

Table 1.1 Main FTU parameters.

avoid damages to the coils. For this reason the machine is contained in a cryostat (Figure 1.3), which is cooled by using liquid nitrogen in order to limit energy requirement and electrical power. The vacuum chamber is fully welded, compact and with walls made of stainless steel AISI304. The internal toroidal limiter and the external poloidal limiter are realised using a molybdenum alloy (TZM). The poloidal section is circular. The machine has a total height of 3 m, a diameter of 5 m and a total weight of 90 t.

An essential element in fusion devices are the plasma diagnostics, used for the machine security, plasma control and physics investigations. The measurements of the main parameters like current, safety factor, plasma vertical position are crucial to avoid damages to the first wall components and predict disruptions. Some of the main important diagnostics are: Fission Chamber, Hard X-ray, BF3 chambers, pick-up coils, Thomson scattering, vloop coils. More details of

the diagnostics are provided in [14], and more information about the diagnostics installed in FTU ports can be found in [15].

1.3 Thesis outline

The common thread of the whole thesis is to provide a contribution to make the nuclear fusion process self-sustainable. At the present time, the possibility to obtain a self-sustained fusion reaction is far from being realised. Plasma fusion performances are hindered from arising of unstable phenomena, since their occurrence often leads to the formation of structured patterns in the relevant measurements and can cause plasma disruptions. As discussed in Section 1.2.4, *edge localized modes* (ELMs) and *runaway electrons* (RE) are two of the most relevant problems in tokamak dynamics, affecting plasma stability.

Due to the severity of the *ELMs* problem in tokamaks, several mitigation techniques have been applied. So far, the most promising strategies are based on the injection of heavy impurities into the plasma, e.g. in the form of pellet. It has been proved that by injecting pellet into the plasma, it is possible to mitigate ELMs. Another approach is the application of a magnetic perturbation allowing to control the dynamics of the system. However, running fusion experiments may be expensive and time-consuming. The most straightforward alternative approach to investigate fusion plasma behaviour is exploiting analogies with other physical systems, whose models are defining according to similar mathematical relationships. In the

first part of the work, a *qualitative low dimensional model of plasma instabilities* [9] has been the focal point. The principal aim is to apply the analogue system approach, in order to design an *electrical analogue* of the plasma behavioural model. The circuit implementation is affected by unavoidable linear and dissipative effects due to the analog devices used. Nevertheless, these effects made more realistic the model of the plasma behaviour, including effects of noise and nonideal behaviours that are always present in real systems. The qualitative model allows to investigate the occurrence of ELMS and to test suitable control strategies. The control consists of avoiding the system to go towards the critical oscillatory regime characterising the occurrence of ELMs. The control strategies are applied directly, in open loop, in the case of *thermostat control* and introducing a feedback, in the case of *pellet injection*, designing an hybrid system. Additionally, the *jerk form* of the model is investigated, in order to understand if it can be useful to easily study the system dynamics. The possibility to model real complex phenomena using very simple analog nonlinear electronic circuits is a powerful tool in the nuclear fusion context. The approach followed enables to carry out various experiments in the circuit by changing the real parameters of the original system by means of low cost resistors. In this way, instead of using a numerical model, the plasma dynamical behaviour can be studied with low cost electronics components.

Another main concerns in tokamak plasma are *runaway electrons* (RE). A beam of fast electrons could reach in ITER current values of $13MA$, causing unrecoverable damages to the tokamak first wall components. In order to mitigate RE, different strategies have

been developed. However, efficient RE control and mitigation techniques require information on RE dynamics. The main data are the RE pitch angle, energy and radial localisation, ideally in real time. As explained in Section 1.2.3, by following a statistical approach such information can be used in the probability distribution, known as distribution function, in order to localise the runaway electrons. The thesis contributes to the improvement of runaway electron control tools, in particular by focusing on diagnostic techniques to extract information on the runaway electron distribution function.

The first part of the work on runaway electrons is the implementation of an *automatic platform* exploiting advanced-image techniques for the RE pitch angle calculation. The work is based on the collaboration with the research group from FTU tokamak experiments. The synchrotron radiation emitted by runaway electrons in FTU is collected by videocameras and spectrometers in the visible and infrared range (Runaway Electron Imaging and Spectroscopy System (REIS) [16]). The visible images of RE synchrotron emission are analysed in order to infer the pitch angle of the observed RE shapes [17–19]. Such data, when combined with the analysis of synchrotron spectra, can provide a better evaluation of the RE energy distribution function and the consequent improvement of RE control strategies.

The second part of the work on runaway electrons is focused on the modelling of the RE dynamics. This work is carried in collaboration with the research group of Frascati and the Plasma Theory research group of Chalmers University of Technology, Gothenburg, Sweden. The diagnostic tool SOFT (Synchrotron-detecting Orbit Following Toolkit) [20] is used to simulate the video images of synchrotron

radiation emitted by runaway electrons in FTU. The diagnostic simulation by SOFT is based on a simplified model, known as cone model, that allows to obtain good approximation of the physical behaviour, reducing the computational costs. Unlike other models, SOFT takes into account different aspects that affect the detected radiation. A parallel study of images and spectra was carried by comparing simulations with experimental data. This work, still ongoing, provides a more precise determination of the runaway electron distribution function parameters.

The thesis is enriched with an additional thematic, based on a research activity performed in collaboration with a research group from Universitat Politècnica de Catalunya, Terrassa, Barcelona, Spain. The remote recovery of audio signals from silent video of the optical speckle patterns has been analysed experimentally. Six different signal recovery algorithms were analysed and compared. The techniques investigated can be a basis for future applications in fusion imaging diagnostics to infer direct plasma measurements from indirect measurements.

The thesis is organised as follows. Chapter 2 presents an experimental setup based on an analog circuit implementation of a minimal model of fusion plasma behaviour. Two nonlinear control approaches to mitigate ELMs, pellet injection and thermostat control, are opportunely designed and investigated. The jerk form of the minimal model is also investigated. Chapter 3 describes an automatic platform exploiting an advanced image-processing technique applied to synchrotron radiation images produced by runaway electrons in a tokamak plasma. The technique is used for the estimation

of the pitch angle of RE in FTU discharges. Chapter 4 presents a more comprehensive analysis of the above synchrotron radiation images by comparing simulations with experiments. The SOFT simulation toolkit has been used. The analysis includes information from synchrotron images as well as synchrotron spectra. RE energy and pitch angle have been determined. Chapter 5 reports a comparative study of audio signal remote recovery algorithms. The audio signals are reconstructed from silent videos of optical speckle pattern. Finally, Chapter 6 draws the conclusion of the overall thesis work.

Chapter 2

Nonlinear circuits to model and control plasma instabilities

2.1 Introduction

During the last decades, *plasma behaviour* has been deeply explored. One of the most interesting phenomena occurring during the nuclear fusion process are *nonlinear unstable phenomena*. Controlling nonlinear phenomena is crucial in many real-world applications [21]. Nonlinearity is essential in the process of modelling physical systems, in particular the ones where the spatial dynamics are important as the temporal dynamics. The nature of these systems generates the conditions in which chaos and nonlinear oscillations may occur. Generally, the complex behaviour is treated as a drawback, for this

reason control strategies to mitigate the chaotic dynamics are used. In control theory, nonlinear system control is fundamental. Different methods and approaches have been designed in order to suppress chaos. Among these plethora of methods, can be mentioned robust adaptive control [22], sliding mode control [23], Lyapunov based approaches [24].

Another type of approach is the *antichaos control strategy*, in which the undesired state of the system is associated to nonlinear oscillations and chaos dynamics did not emerge. The normal operating condition of the system is associated to the chaotic behaviour. This is the case of the physical model under study.

Over the years, several models have been presented in order to reproduce the dynamical behaviour of the plasma. The thesis work focuses on a *low dimensional model* [25], presented in [9], describing the quasi-periodic plasma dynamics.

Operating under high confinement regime (H-mode) allows to obtain an higher energy confinement time, however nonlinear unstable phenomena can occur, such as *edge localized modes* (ELMs). Investigate the physical formation and development of ELMs is one of the main challenges in nuclear fusion field. These kind of instabilities may lead to severe damages to the vessel wall components due to their extremely high energy transfer rate. As a consequence, a low-dimensional modelling of ELMs dynamics is useful to qualitative understand the effect of driving parameters allowing to design suitable control strategies.

The bifurcation properties of the system have been studied by varying two independent parameters. The dynamical regions found are

remarkably rich. According to the minimal model of the *sawtooth oscillations* presented in [26], it is shown that, in the appropriate parameter regime, it is characterised of limit-cycle behaviour resembling ELMs. Despite its simplicity, the low dimensional model [9], used in the case under examination allows to obtain predictions that qualitative match the experimental behaviour of ELMs.

Two nonlinear control techniques will be investigated [27] and applied to the model [9], in order to control the dynamical behaviour of the system and to prevent the dynamical regime corresponding to ELMs phenomenon. The approach followed involves to design and test the circuit analogue implementation of the minimal model of plasma instabilities. The electronic circuit implemented follows the same dynamical equations of the model. Understanding the main features of the plasma quantities and the instabilities occurrence can be very powerful to control the overall process and set up the confinement time.

2.2 Plasma lower dimensional model

The minimal model introduced by Constantinescu *et al.* [9] describes the interaction between two macroscopic quantities: the plasma pressure and the magnetic field. The dynamical model allows to represent complex phenomena, based on the interplay between the energy conservation and the relaxation dynamics. The first one models the pressure gradient behaviour and it is the driving part of the system, instead the relaxation dynamics are related to the instability phenomena.

2.2.1 The dynamical model

The normalized dimensionless dynamical system reads as follow:

$$\begin{aligned}\dot{x} &= (z - 1)y - \delta x \\ \dot{y} &= x \\ \dot{z} &= \eta(h - z - y^2 z)\end{aligned}\tag{2.1}$$

where ξ is the magnetic field ($x = \xi$, $y=k\xi$), p is the pressure gradient ($z=p$). The model qualitative describes the dependence from three bifurcation parameters: δ is the dissipation/relaxation of perturbation related to the ELMs burst, η represents the heat diffusion coefficient and h is the normalized input power of the system, that induces ELMs burst.

A very interesting feature of the system is that above a critical input threshold of the power ($h > 1$), the system can undergo instabilities processes. As a consequence, h has been set equal to 1.5, so that the dynamical zones can be evaluated by varying the independent parameters, namely δ and η .

2.2.2 Circuit implementation

The circuit design and implementation was performed in agreement with the minimal model 2.1, by following the state variable approach [28]. The analog circuit implementation involves the use of ideal components, which includes standard passive elements (capacitors and resistors) and active devices, like operational amplifiers (TL084IN) used to realise algebraic adders and active integrators, and analog

multipliers (AD633) to reproduce nonlinearities.

The equations governing the overall circuit are the following:

$$\begin{aligned}\dot{x} &= \frac{1}{R_{C1}C_1} \left[\left(\frac{R_{F1}}{R_1} - 1 \right) x - \frac{R_{F1}}{R_2} y + \frac{R_{F1}}{R_3} V^* \right] \\ \dot{y} &= \frac{1}{R_{C2}C_2} \left[\frac{R_{F2}}{R_4} x + \left(\frac{R_{F2}}{R_5} - 1 \right) y \right] \\ \dot{z} &= \frac{1}{R_{C3}C_3} \left[\frac{R_{F3}}{R_7} V - z - \frac{R_{F3}}{R_6} V^{**} \right]\end{aligned}\tag{2.2}$$

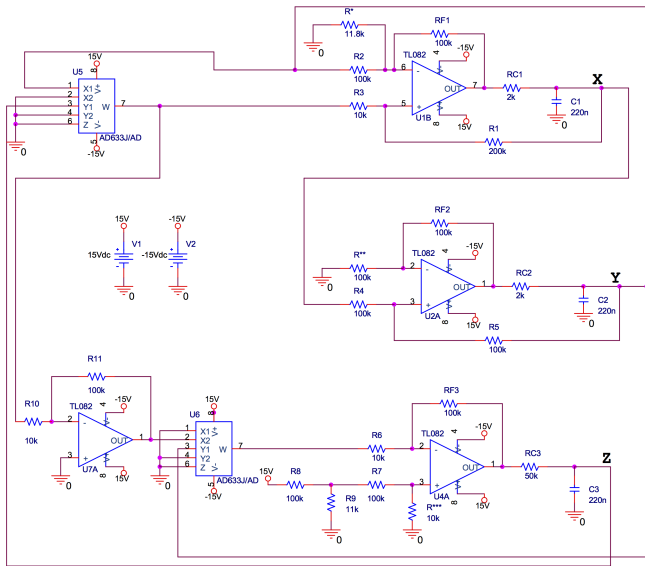
$$\text{where } V^* = \frac{yZ}{10}, V = 15V, V^{**} = \frac{y^2Z}{10}.$$

Figure 2.1a shows the electrical scheme of the circuit, designed by using the software OrCAD. In the preliminary implementation of the circuit, the bifurcation parameters have the following values: $h = 1.5$, $\eta = 0.01$ and $\delta = 0.5$. During the test phase, the η parameter is associated to a potentiometer in order to investigate the dynamical zones for various type of oscillations. The values of the components are chosen in order to match the minimal model 2.1 with the circuit equations 2.2:

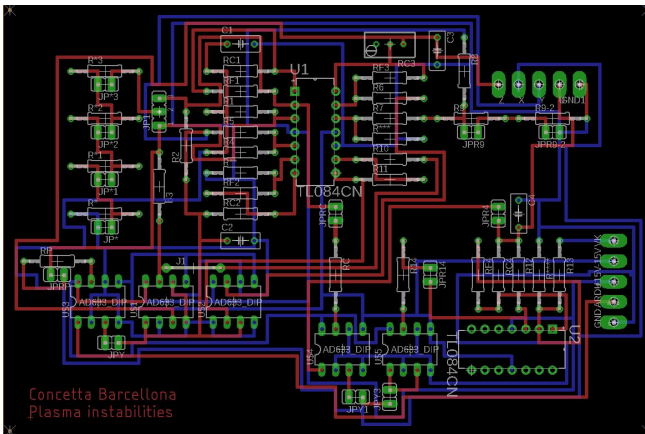
$$\begin{aligned}R_1 &= 200k\Omega, R_2 = 100k\Omega, R_3 = 10k\Omega, R^* = 11.8k\Omega, R_4 = 100k\Omega, R_5 = \\ &100k\Omega, R^{**} = 100k\Omega, R_7 = 100k\Omega, R^{***} = R_6 = 10k\Omega, R_7 = 100k\Omega, \\ &R_8 = 100k\Omega, R_9 = 11k\Omega, R_{10} = 10k\Omega, R_{11} = 100k\Omega, R_{F1} = R_{F2} = \\ &R_{F3} = 100k\Omega, R_{C1} = R_{C2} = 2k\Omega, C_1 = C_2 = C_3 = 220nF.\end{aligned}$$

The independent parameter η was implemented through resistors

R_{C1} and R_{C3} according to the relationship $\eta = \frac{R_{C1}}{R_{C3}}$. In order to investigate the different dynamical behaviours that can be obtained by varying η , R_{C3} was implemented using a potentiometer with nominal value equal to $100k\Omega$. The circuit was, initially, realised on a breadboard, by using discrete off-the-shelf components, as shown in Figure 2.2a.



(a)



(b)

Figure 2.1 (a) Circuit diagram of the electronic circuit. (b) PCB layout.

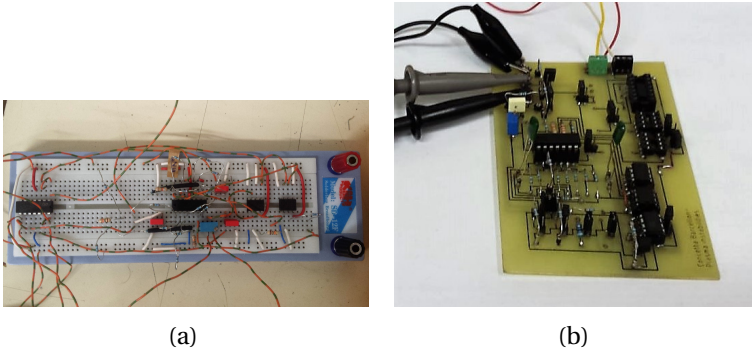


Figure 2.2 (a) Nonlinear circuit implementation on breadboard. (b) Nonlinear circuit implementation on PCB.

After the initial test done on a breadboard, a Printed Circuit Board (PCB) was realised. In Figure 2.1b is shown the PCB layout, designed using Eagle software. Figure 2.2b presents the physical implementation of the PCB circuit.

2.2.3 Dynamical regions and behaviour

By varying the independent parameter η , the circuit dynamical zones were obtained.

Following [9], the ELMs regime corresponds to sawtooth-like periodic oscillations, while the chaotic behaviour is associated to the reduction of the edge pressure gradient, thus mitigating the onset of the instability [29].

The simulations were performed using MATLAB software. The orbit starts at initial conditions $(x_0, y_0, z_0) = (0, 1.7, 1.01)$, according to the studies performed in [9]. Signals were acquired by using a

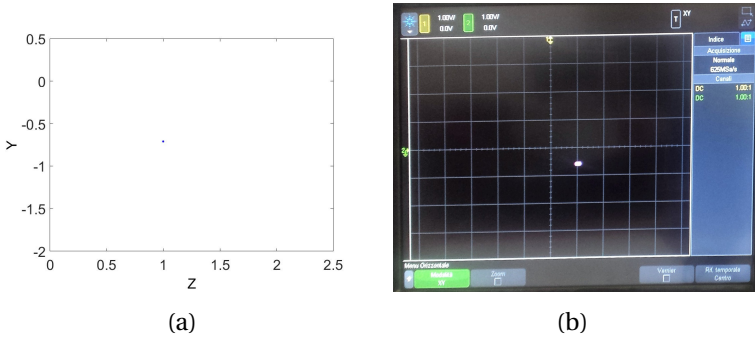
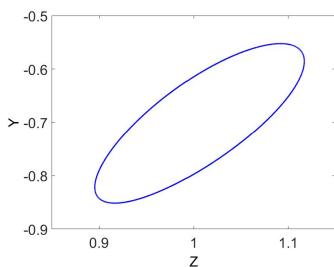


Figure 2.3 Damped oscillations $(\delta, \eta) = (0.5, 0.668)$.

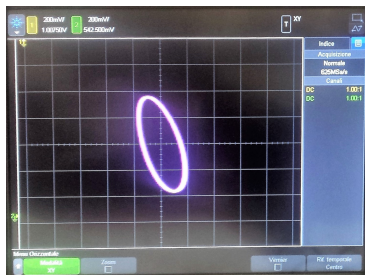
National Instrument data acquisition board with a sampling frequency equal to $50kHz$ and processed in LabVIEW environment. Four dynamical zones for various type of oscillations can be distinguished: damped oscillations $(\delta, \eta) = (0.5, 0.668)$, periodic oscillations $(\delta, \eta) = (0.5, 0.55)$, chaotic oscillations $(\delta, \eta) = (0.5, 0.08)$ and ELMs oscillations $(\delta, \eta) = (0.5, 0.011)$. Figures 2.3, 2.4, 2.5 and 2.6 show a comparison between simulations results and oscilloscope traces of the attractor on yz -plane.

The bifurcation diagram explores the dynamical behaviour of the system when a control parameter is varied. Generally, numerical methods are used to elaborate bifurcation diagrams [22]. The mathematical model of the system 2.1 includes a rich bifurcation scenario, as demonstrated in the analysis carried out in [30].

For a quantitative characterisation of chaos, the spectrum of Lyapunov exponents is studied. The Lyapunov exponents quantify the high sensitivity of chaotic systems to initial conditions [22]. The Lyapunov spectrum was calculated according to the method in [31],

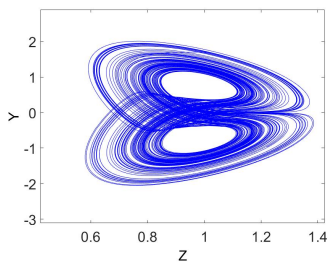


(a)

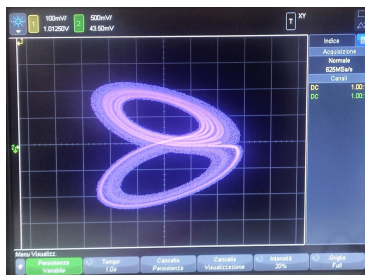


(b)

Figure 2.4 Periodic oscillations $(\delta, \eta) = (0.5, 0.55)$.



(a)



(b)

Figure 2.5 Chaotic oscillations $(\delta, \eta) = (0.5, 0.08)$.

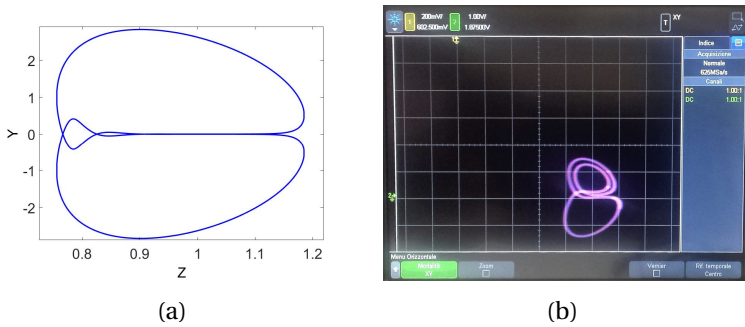


Figure 2.6 ELMs oscillations $(\delta, \eta) = (0.5, 0.011)$.

using a total integration time $T = 1000$ and step size $\Delta t = 0.01$.

The behaviour of the system under examination was explored by varying at small steps the bifurcation parameter η . Figure 2.7 shows the dynamical behaviour analysis of the system 2.1. In Figure 2.7(a) and Figure 2.7(b) the numerical and experimental bifurcation diagrams with respect the η parameter are presented. The two diagram show the local minima and maxima of the z variable.

The three Lyapunov exponents, shown in Figure 2.7(c), confirm that the attractor is chaotic for $\eta = 0.08$.

Because of the physical meaning of the considered model, a control strategy which involves the injection of an external driving signal was investigated.

2.3 Pellet injection

During real nuclear fusion campaigns, instabilities can be mitigated by injecting pellet at given rates inside the vacuum chamber. Pellet

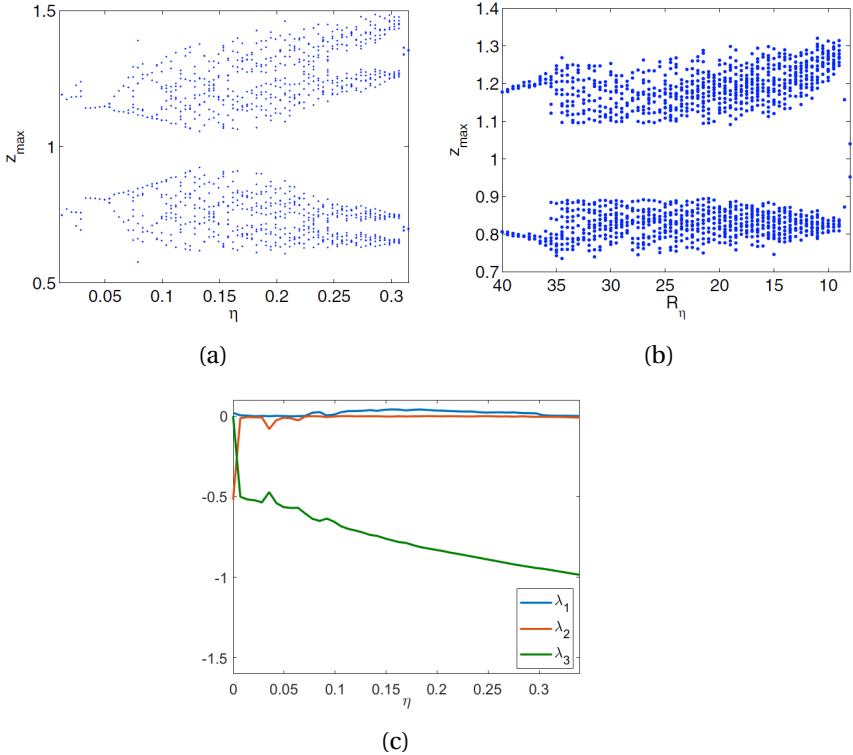


Figure 2.7 Analysis of the dynamical behaviour of the system 2.1 with respect to the parameter η . (a) Simulated bifurcation diagram (b) Experimental bifurcation diagram (c) Lyapunov spectrum.

injection can be defined as an open-loop control strategy in which an external pulse signal is applied [9], [22]. An hybrid analogue model composed of both an analog circuital part and a digital part has been designed, able to model the plasma variables during ELMs and after pellet injection.

2.3.1 The dynamical model

Working on the physical model 2.1, a control strategy based on the injection of an external driving signal is applied. The perturbation term is added on the first equation of the model 2.1:

$$\begin{aligned}\dot{x} &= -\{1 - [z + P(t)]\}y - \delta x \\ \dot{y} &= x \\ \dot{z} &= \eta(h - z - y^2 z)\end{aligned}\tag{2.3}$$

The perturbation $P(t)$ that represents the pellet injection can be simulated by the following expression:

$$P(t) = a * \exp\{-[t - t_{period} \text{int}(t/t_{period}) - \delta_P]^2/b\}\tag{2.4}$$

where a is the perturbation amplitude, t_{period} is the perturbation period, δ_P is the perturbation shift, and b is the perturbation width. The function int indicates the integer part of the argument. In order to work in the ELMs region the following parameters are chosen: $h = 1.5$, $\delta = 0.5$, $\eta = 0.009$. In the case under examination, the control parameters are the pulse frequency, width and amplitude. The perturbation parameters set are the following: $a = 5$, $t_{period} = 5$, $\delta_P = 2$ and $b = 2$.

2.3.2 Circuit implementation

The circuit design and implementation is modified in order to match with equation 2.3. Referring to the equation 2.2 regarding the overall circuit, the first equation is modified as follows:

$$\dot{x} = \frac{1}{R_{C1} C_1} \left[\left(\frac{R_{F1}}{R_1} - 1 \right) x - \frac{R_{F1}}{R_2} y + \frac{R_{F1}}{R_3} V^* + \frac{R_{F1}}{R_P} \frac{P(t)y}{10} \right] \quad (2.5)$$

with $R_P = 111.4k\Omega$, and $R^* = 9.6k\Omega$. The capacitors values of the circuit are set in the following way $C_1 = C_2 = C_3 = 10nF$, in order to have comparable frequencies with the perturbation. The perturbation term is added to the circuit by using an AD633 multiplier, as shown in the electrical scheme in Figure 2.8.

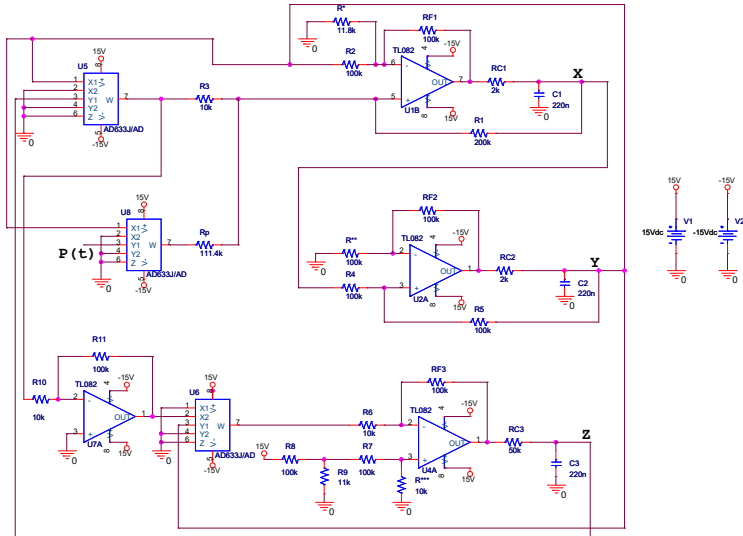


Figure 2.8 Circuit diagram in the case of pellet injection.

The perturbation $P(t)$ is generated by using a microcontroller board Arduino[®] Uno [32]. It is a robust multipurpose board, that can be used for coding and work with electronics. The perturbation is coded as an 8-bit word. The digital output is converted to analog voltage through an R-2R converter and sent to the overall circuit.

2.3.3 Results

Figure 2.9 and Figure 2.10 show the resulting temporal dependence of the pressure gradient. Two different regions have been investigated: before and after pellet injection. In particular, Figure 2.9 shows the dynamical behaviour of the z variable in ELMs conditions by considering both simulations and experimental results.

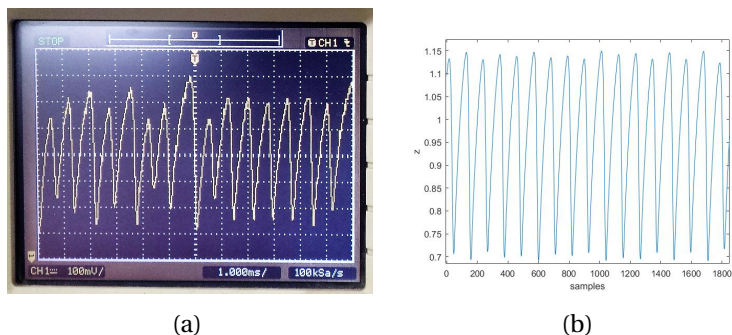


Figure 2.9 Experimental trend of z variable before pellet injection.

The dynamical trend is quasi-periodic as expected in the case of ELMs in a real nuclear fusion reaction. The dynamical evolution of the plasma pressure gradient radically changes when the pellet injection is activated. The system behaviour pass from ELMs regime to chaotic region, as shown in Figure 2.10.

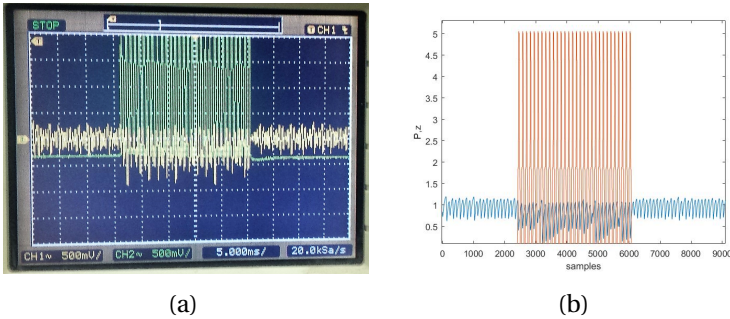


Figure 2.10 Experimental trend of ELMs during pellet injection ($\eta = 0.5$ and $t_{period} = 50$). Perturbations $P(t)$ are shown by green lines in the case (a) and by red lines in the case (b).

The chaotic dynamics obtained in the case of ELMs mitigation is confirmed by the literature [33], [29]. Figure 2.11 and Figure 2.12 show the attractors on the zy -plane before and after pellet injection. The experimental attractors are in agreement with the numerical results.

Based on the results, it is possible to conclude that the perturbation affects the plasma stability changing the plasma variables regime and increases the ELMs frequency. The t_{period} parameter has been investigated. Based on the perturbation expression 2.4, it can be notice that the t_{period} changes the signal frequency, as is shown in figure 2.13 ($t_{period} = 35$). As a consequence, increasing the t period, the frequency of the perturbation signal decrease thus leading to a more slighter effect on the ELMs.

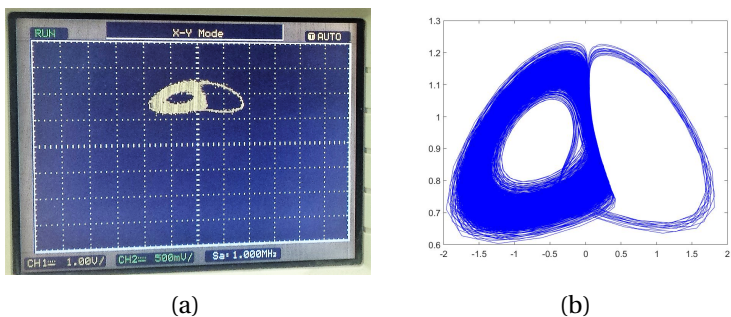


Figure 2.11 Experimental trend of the attractor on the zy -plane before pellet injection.

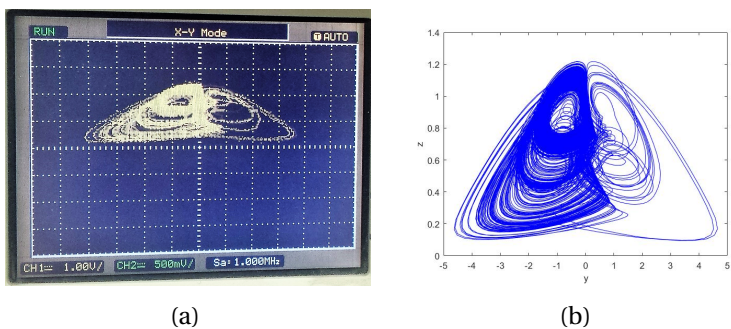


Figure 2.12 Experimental trend of the attractor on the zy -plane after pellet injection.

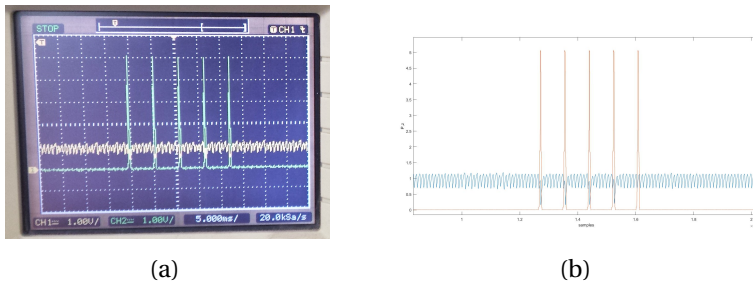


Figure 2.13 Experimental trend of ELMs with pellet injection by varying the parameter t_{period} . Perturbations $P(t)$ are shown by green lines in the case (a) and by red lines in the case (b).

2.4 Thermostat control

Another approach to control the dynamical behaviour of the system is based on the introduction of a feedback which regulates the frequency and the amplitude of an external control signal. It is a similar situation to the known thermostat control, investigated by Nosé [34], Hoover [35]. An analogous approach has been followed by Constantinescu *et al.* [33], where was adopted an open-loop scheme, in which an external magnetic perturbation has been applied as a pulse to the model 2.1. In our case, a closed-loop strategy is followed using the thermostat control.

2.4.1 The dynamical model

The closed-loop control approach exploit the thermostat control. Based on the model of the system 2.1, a feedback is added through an additional dynamical variable that mediates between the control

action and the behaviour of a state variable. The system of equation obtained is the following:

$$\begin{aligned}
 \dot{x} &= (z - 1)y - \delta x - ux \\
 \dot{y} &= x \\
 \dot{z} &= \eta(h - z - y^2 z) \\
 \dot{u} &= x^2 - k
 \end{aligned} \tag{2.6}$$

This method uses the same structure of the Nosé-Hoover oscillator, in order to obtain the thermostat control, see Sprott *et al.* [36]. From a physical point of view, we can consider that a magnetic perturbation acts on the system, as can be seen in 2.6, where the δ parameter is varied by the thermostat control. In order to work in the ELMs dynamical region the following parameters are set: $\delta = 0.5$, $\eta = 0.009$, and $h=1.5$. The control parameter k varies in the range [0-1].

2.4.2 Circuit implementation

The circuit implementation 2.2 is modified in order to match with the model 2.6. Respect to the equations 2.2, a fourth equation corresponding to the new state variable is added and his contribution appears in the first equation:

$$\begin{aligned}
 \dot{x} &= \frac{1}{R_{C1}C_1} \left[\left(\frac{R_{F1}}{R_1} - 1 \right) x - \frac{R_{F1}}{R_2} y + \frac{R_{F1}}{R_3} V^* - \frac{R_{F1}}{R_C} V_C \right] \\
 \dot{u} &= \frac{1}{R_{C4}C_4} \left[-\frac{R_{F4}}{R_{10}} V_k + \frac{R_{F4}}{R_{11}} V^{***} + \left(\frac{R_{F4}}{R_{12}} - 1 \right) u \right]
 \end{aligned} \tag{2.7}$$

where: $V_C = \frac{uX}{10}$, $V^{***} = \frac{x^2}{10}$, $R_C = 10k\Omega$, $R^* = 67k\Omega$, $R_{F4} = R_{10} = R_{12} = 100k\Omega$, $R_{11} = 10k\Omega$, $R^{***} = 11k\Omega$, $C_1 = C_2 = C_4 = 10nF$, $C_3 = 470nF$, $RC_3 = 4k\Omega$ (the components values not specified are the same of the first implementation shown in 2.2). Figure 2.14 shows the electrical scheme of the overall circuit.

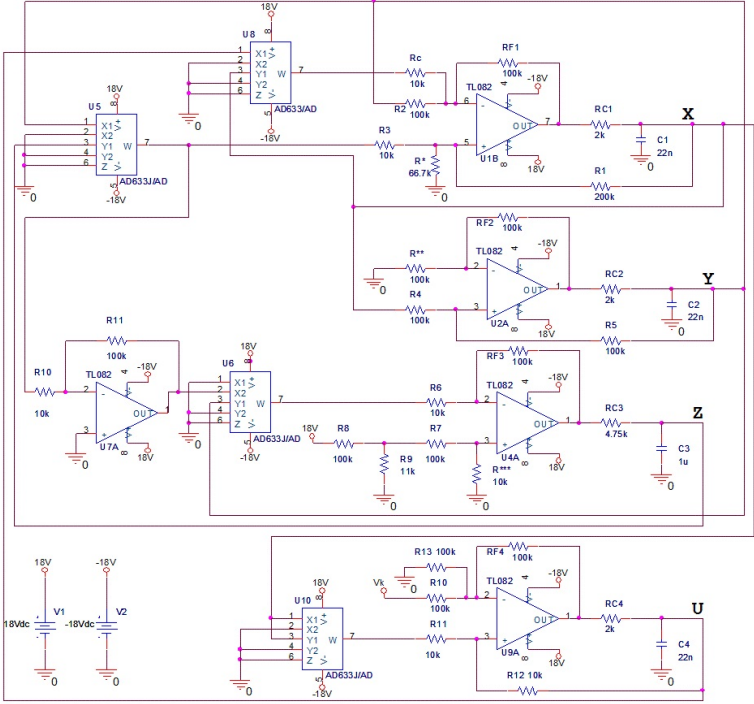


Figure 2.14 Circuit diagram in the case of thermostat control.

2.4.3 Results

It is possible to pass from ELMs region to the chaotic dynamical behaviour changing the control parameter k , as we can see in Figure 2.15. As desired, the average value of z is reduced.

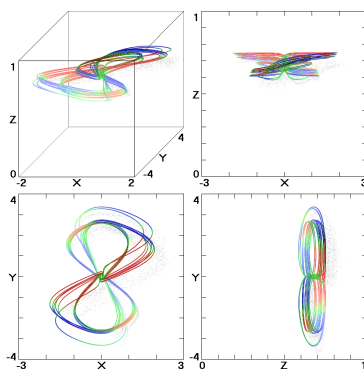


Figure 2.15 Attractors in the case of thermostat control application.

In order to observe the complete variety of dynamical behaviours of the system, the bifurcation diagram has been analysed. Figure 2.16 shows a comparison between the simulated and experimental bifurcation diagrams of z variable respect to the control variable k . From the analysis of the results, it is possible to conclude that the experimental data are in line with the simulated values.

2.5 The Jerk dynamics

In the last years, scientists focus on the study of chaotic oscillators based on jerk equations [37]. This type of oscillators can be defined by third order differential equations in the form $\ddot{x} = f(\ddot{x}, \dot{x}, x)$ [38],

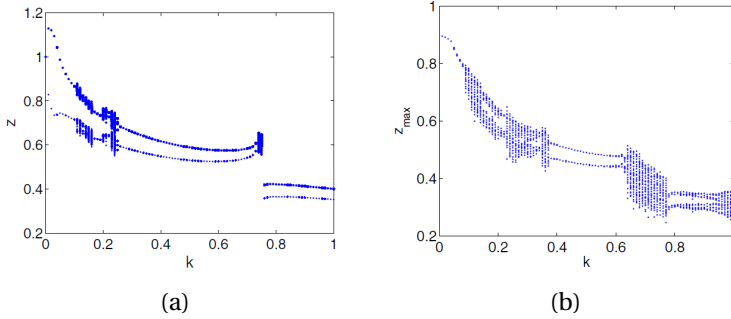


Figure 2.16 Bifurcation diagrams with respect to the control parameter k (a) Simulated diagram. (b) Experimental diagram.

[39], [40]. The jerk equations formulation allows to create *elegant* models of chaotic circuit, as defined in [41]. Another advantage is the design of electronic chaotic circuits in simple autonomous dissipative systems [42]. In the case under examination, the procedure to derive the jerk form of the plasma lower dimensional model 2.1 has been followed. It has been proved that the jerk form of the system can be obtained for the variable y , while for the variables x and z it can't be found. Based on the jerk equations obtained, the corresponding electronic circuit has been realised, in order to investigate the dynamical behaviour.

2.5.1 The Jerk Form of plasma instabilities model

Let us consider the qualitative model of plasma instabilities 2.1. The target is to verify if it is possible to obtain the following jerk forms:

$$\ddot{x} = f_1(\ddot{x}, \dot{x}, x) \tag{2.8}$$

$$\ddot{y} = f_2(\ddot{y}, \dot{y}, y) \quad (2.9)$$

$$\ddot{z} = f_3(\ddot{z}, \dot{z}, z) \quad (2.10)$$

The Eq. 2.9 form is obtained in our specific case. In order to prove the existence of 2.9, the first step is to differentiate once the first equation of system 2.1:

$$\ddot{x} = \dot{z}y + zy\dot{} - \dot{y} - \delta\dot{x} \quad (2.11)$$

and to differentiate twice the second equation of system 2.1:

$$\ddot{y} = \ddot{x} \quad (2.12)$$

Eq. 2.11 is substitute in Eq. 2.12:

$$\ddot{y} = \dot{z}y + zy\dot{} - \dot{y} - \delta\dot{x} \quad (2.13)$$

From the combination of the first and second equations of system 2.1 it has been obtained:

$$z = \frac{\ddot{y} + y + \delta\dot{y}}{y} \quad (2.14)$$

Substituting the first and third equations of system 2.1 and the Eq. 2.14 in Eq. 2.13, the result obtained, after some simplifications, is the following:

$$f_2(\ddot{y}, \dot{y}, y) = (-\eta - \eta y^2 + \frac{\dot{y}}{y} - \delta)\ddot{y} + (-\eta\delta - \eta y^2\delta + \delta\frac{\dot{y}}{y})\dot{y} + (\eta h - \eta - \eta y^2)y \quad (2.15)$$

Once obtained the jerk expression 2.15 corresponding to Eq. 2.9, the state space normal form has been derived. For the jerk system 2.9 in state space normal form, the subsequent set of state variables has been considered:

$$\tilde{X} = \begin{bmatrix} \tilde{x} \\ \tilde{y} \\ \tilde{z} \end{bmatrix} \quad (2.16)$$

The following relations apply:

$$\tilde{x} = y, \quad \tilde{y} = \dot{y}, \quad \tilde{z} = \ddot{y} \quad (2.17)$$

By differentiating it is obtained:

$$\dot{\tilde{x}} = \dot{y} = \tilde{y}, \quad \dot{\tilde{y}} = \ddot{y} = \tilde{z}, \quad \dot{\tilde{z}} = \dddot{y} = f_2(\ddot{y}, \dot{y}, y) = f(\tilde{z}, \tilde{y}, \tilde{x}) \quad (2.18)$$

By using Eq. 2.15, the following transformations are obtained:

$$\begin{aligned} \tilde{x} &= \tilde{y} \\ \tilde{y} &= \tilde{z} \\ \dot{\tilde{z}} &= (-\eta - \eta\tilde{x}^2 + \frac{\tilde{y}}{\tilde{x}} - \delta)\tilde{z} + (-\eta\delta - \eta\tilde{x}^2\delta + \delta\frac{\tilde{y}}{\tilde{x}})\tilde{y} \\ &\quad + (\eta h - \eta - \eta\tilde{x}^2)\tilde{x} \end{aligned} \quad (2.19)$$

Jerk equations 2.19 represent in different state representation the system 2.1 and keep the same structural properties [43]. The independent parameters values $h = 1.5$ $\delta = 0.5$, $\eta = 0.009$ are chosen in order to work in ELMs region. The strategy followed involves the addition of a controller kz in the third equation of the expression 2.19. From the analysis performed, it has been found that for specific

values of the controller, the system goes from ELMs regime to the desired chaotic behaviour, as shown in Figure 2.17.

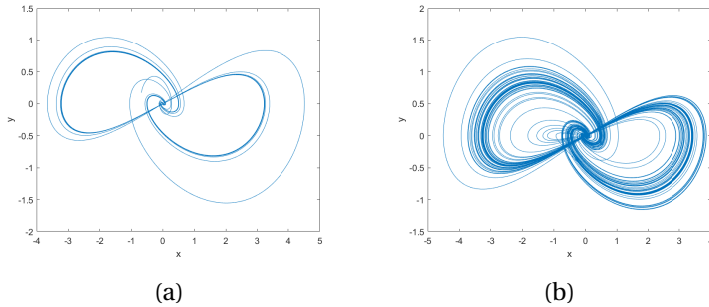


Figure 2.17 Attractors of plasma minimal model in jerk form (a) ELMs regime ($k=0$). (b) Chaotic behaviour ($k=0.002$).

2.5.2 Circuit implementation

Starting from the jerk equations 2.19 found, an electronic circuit was designed and implemented. The circuital equations are the

following:

$$\begin{aligned} \dot{x} &= \frac{1}{R_{C1}C_1} \left[\frac{R_{F1}}{R_{11}} y + \frac{R_{F1}}{R_{12}} x - x \right] \\ \dot{y} &= \frac{1}{R_{C2}C_2} \left[\frac{R_{F2}}{R_9} z + \frac{R_{F2}}{R_{10}} y - y \right] \\ \dot{z} &= \frac{1}{R_{C3}C_3} \left[\frac{R_{F3}}{R_1} z - z + \frac{R_{F3}}{R_2} V_1 - \frac{R_{F3}}{R_3} V_2 - \frac{R_{F3}}{R_4} \frac{y}{100} \right. \\ &\quad \left. - \frac{R_{F3}}{R_5} V_3 + \frac{R_{F3}}{R_6} V_4 + \frac{R_{F3}}{R_7} \frac{x}{100} - \frac{R_{F3}}{R_8} \frac{x^3}{100} \right] \end{aligned} \tag{2.20}$$

where $R_1 = 203K\Omega$, $R_3 = R_8 = 111k\Omega$ $R''_4 = R''_7 = 1k\Omega$, $R_4 = R_5 = R_7 = 222k\Omega$, $R_6 = 200k\Omega$, $R^{***} = 79.4k\Omega$, $R_{F1} = R_{F2} = R_{F3} = R_2 = R'_4 = R'_7 = R_9 = R_{10} = R^{**} = R_{11} = R_{12} = R^* = 100k\Omega$ $C_1 = C_2 = C_3 = 10nF$, $R_{C1} = R_{C2} = R_{C3} = 2k\Omega$, $C = 0.1\mu F$.

The values of the components have been chosen in order to match Eq. 2.19 with Eq. 2.20. In particular, the algebraic adders are realised using one operational amplifier (TL084IN) and the nonlinearity are reproduced using analog multipliers (AD633) and analog divider (AD734ANZ). Figure 2.18 shows the electrical scheme of the jerk circuit.

The circuit has been implemented by using off-the-shelf discrete components, as shown in Figure 2.19.

Several tests have been carried out in order to reproduce the dynamical behaviour of the system. However, there was a problem in the divider configuration, because the variable values comprises the zero and gives numerical errors. The circuit showed a bistable behaviour,

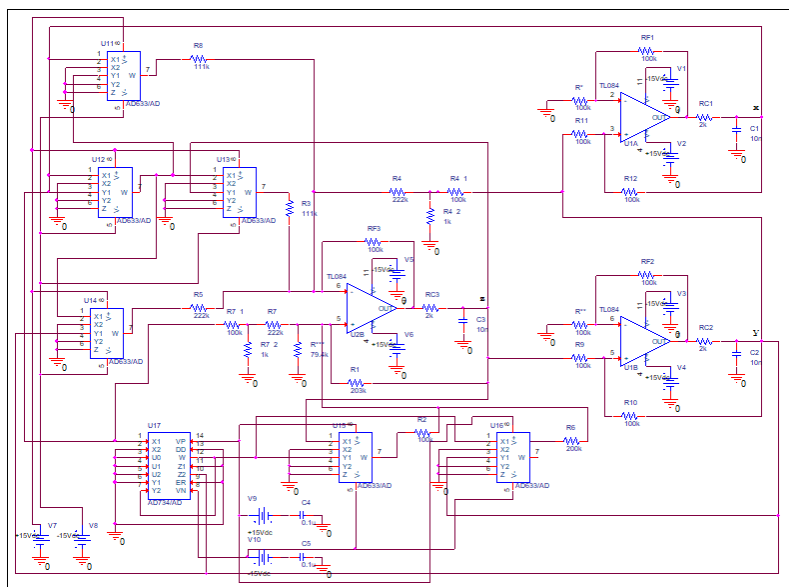


Figure 2.18 Circuit diagram of the plasma model in jerk form.

for this reason the expected behaviour has been obtained only in some cases. It is possible to conclude that the jerk form of plasma lower dimensional model is more complicated from a circuitual point of view and gives numerical errors.

2.6 Conclusion

The possibility to model complex phenomena, that have been discovered in tokamak machine, by using very simple analog nonlinear electronic circuits is a fundamental topic in nonlinear science. In this chapter, a low dimensional model describing the quasi-periodic

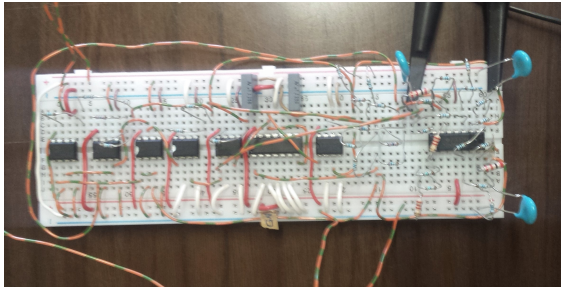


Figure 2.19 Jerk plasma lower dimensional model circuit.

plasma dynamics observed in nuclear fusion experiments has been investigated. The model is able to reproduce the behaviour of magnetic variables inside the vacuum chamber of a fusion reactor, catching the dynamical properties of plasma instabilities. In the phase portrait of the model, the unwanted behaviour is associated to a stable limit cycle, while a chaotic behaviour is needed to drive away from instabilities. For these reasons an antichaos control strategy must be adopted for this system.

An experimental setup based on an analog circuit implementation of the model is introduced. The need of modelling and controlling plasma instabilities ELMs is related to the implementation of an analogue qualitative model that can be useful to fine-tune the ideal physical model in time. A circuit design and implementation includes nonidealities and unavoidable component tolerances, allowing to take into account the nonideality of the phenomenon. This approach is completely different from considering a numerical model. An higher level of representation in the model may increase the complexity of the model itself, instead working with a real device

allows to test the robustness of the proposed control technique with respect to distinct sources of uncertainty, maintaining a reasonable level of complexity. By using a digital simulator it is possible to test the validity of the model design, but not its robustness.

From the results obtained, it has been possible to identify the parameters that can be adopted to control ELMs suppression by acting on pellets perturbations and on the control parameter k . In both cases very simple and low cost analog/digital devices are used. The experimental results obtained confirm the validity of this approach, allowing to test the dynamical behaviour of the system without the need of running a real nuclear fusion experiment. It is very useful from a qualitative point of view to have a very simple circuit, but with a very complex behaviour that reproduce exactly the original real system. The analog model implementation paves the way towards a more complex issue that is the identification and control of nonlinear phenomena during nuclear fusion experiments. Simulations and software techniques are powerful tools in the nuclear fusion field. In particular, in the next chapter, a technique to identify runaway electrons in tokamak machines will be presented.

Chapter 3

Image-Processing for the Estimation of Pitch Angle for Runaway Electrons in Tokamak

3.1 Introduction

Runaway electrons (RE) have been identified in different plasmas, including thunderstorms [44, 45] and solar flares [46]. In a tokamak plasma [47], RE are considered one main threat. A key target of the future reactors is the RE diagnostic and control. An automatic platform for the RE pitch angle estimation, which exploits advanced image-processing technique on the visible images of the RE synchrotron radiation, is presented [48, 49]. Before describing the platform in

detail, the basic theory of runaway electrons, synchrotron radiation and pitch angle estimation will be reviewed.

3.2 Runaway Electrons

Runaway electrons are beams of particles accelerated from a strong electric field to velocities close to the speed of light. Their energy may reach the order of hundred of MeV with current in the order of MA , causing several damages to the first wall components.

In normal operating mode of the tokamak machine, electrons move with a thermal velocity in a equilibrium condition: the toroidal parallel electric field $E_{||}$ accelerates the electrons and the collision with other particles decelerates them. However, instabilities, leading to *disruptions*, rising in tokamak plasma could cool the plasma and dissipate the toroidal current [50, 51]. As a consequence a strong electric field is generated that unbalances the equilibrium condition and accelerates the electrons up to relativistic speed.

Since the 1900's the physics of runaway electrons has been investigated [52] and the first theoretical explanation has been done by the physicist Dreicer [53, 54]. The basic concept is that the friction force of a particle moving faster than the thermal speed, that is the average speed of particles for a particular temperature, is $\propto 1/v^2$, where v is the speed of the particle. If it is applied an electric field the particles will be accelerated and, in absence of other forces, could reach velocity close to the speed of light. The RE theory has been extended to relativistic particles and it has been demonstrated that RE generate if the parallel electric field $E_{||}$ is greater than the critical

electric field E_C [55].

There are two principle mechanisms of RE generation. In addition to the Dreicer mechanism, RE generation can be defined by a 0-D modeling:

$$\dot{n}_{RE} = S_{pri} + \gamma_A(n_{RE}) \quad (3.1)$$

where $S_{pri} = f(T_e, n_e, E_{||}, Z_{eff})$ is the *primary generation (Dreicer)*, due to the continuous electric field acceleration; $\gamma_A(n_{RE})$ is the *secondary generation* or *avalanche* (γ_A is the multiplication factor of the avalanche) [56–59]. In the avalanche process, there is a collision between an highly energetic electron and a thermal electron realising a large amount of energy and turning the thermal electron in a runaway one. The mechanism needs an existing seed of electrons, but when present they multiply exponentially.

Another mechanism is the RE *hot-tail generation* [60, 61]. During a rapid plasma cooling, the electron distribution needs some time to balance to the new temperature. In particular, the fastest electrons take more time to slow down (due to the dynamics of the collisional friction force) and generate a "tail" in the electron energy distribution. This hot tail electrons can be accelerated easily by the electric field and become RE.

3.3 Synchrotron radiation

RE emit *synchrotron radiation* moving at relativistic speeds around magnetic field lines. Synchrotron radiation is defined as the radiation occurring when charged particle are accelerated in a curved path. The radiation emitted is essential as energy loss mechanism [62, 63]

and allows to detect and investigate RE dynamics.

In this thesis, the synchrotron images acquired in FTU [64] have been analysed. The diagnostic used to measure synchrotron radiation is the Runaway Electron Imaging and Spectroscopy System (REIS), a portable device designed for medium size tokamak. The REIS diagnostic consists of a visible camera and spectrometers, described in 3.4, used to collect the fraction of synchrotron radiation emitted in near infrared (IR) and visible wavelengths. When the electron velocity comes close to the speed of light, the relativistic beaming effect induces the emission pattern to collimate forward [65]. For this reason, only the electrons moving towards the camera can be detected. Figure 3.1 shows an example of synchrotron radiation "spot" image, acquired in FTU tokamak.

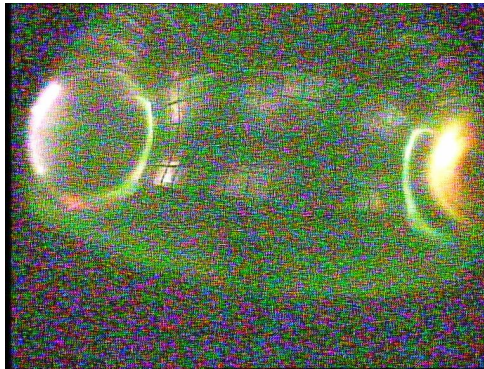


Figure 3.1 Visible light image acquired in FTU during discharge #41750. The spot on the right is the synchrotron radiation emitted by RE.

Analysing visible images it is possible to estimate the most important RE parameters, namely energy and pitch angle, since the shape of the spot varies sensitively according to their values.

3.4 Detection system

The *Runaway Electron Imaging and Spectroscopy System* (REIS) is a wide-angle optical portable diagnostic, designed, developed and realised in ENEA-Frascati laboratories. The system permits the simultaneous detection of the forward and backward Visible (VIS)/Near Infrared (NIR) images and spectra of REs synchrotron radiation. The REIS was mounted on the port #6 of the FTU equatorial plane. The REIS system collects simultaneously data from two lines of sight, as shown in Figure 3.2.

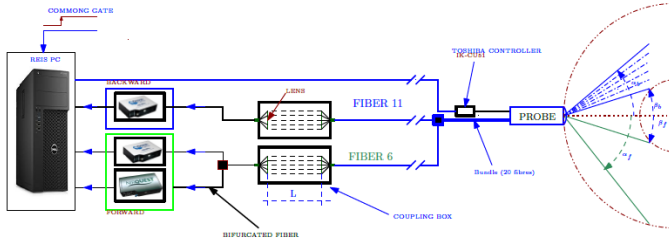


Figure 3.2 Overview of the REIS schematic: the probe head is composed by a wide angle lens coupled, through a set of lenses, to an optical spectrometer for the synchrotron spectra acquisition and by a CCD camera for the visible images acquisition [66].

The visible images of the vessel poloidal cross-section are acquired through a CCD color micro camera at rate of 25 frames per second.

The visible and infrared emission spectra are collected using an incoherent bundle of fiber, in a spectral range spanning from $500nm$ to $5000nm$, in its more recent version (REIS-E). More detailed information on the REIS diagnostic can be found in [64, 16]. Figure 3.3 shows the CCD camera and the objective lens installed in the REIS head.

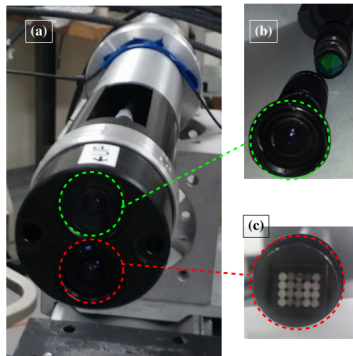


Figure 3.3 REIS head (a) composed by a visible CCD camera system (b) and a 5×4 incoherent fiber bundle array (c).

In particular, the visible images of the vessel cross-section are acquired through a wide-angle objective lens ($f = 3mm$) combined with a visible CCD camera (Toshiba, sensor imaging at 25 fps). The camera sensor's active area is of $5.5mm \times 6mm$. In addition, other two identical CCD visible camera are installed on FTU equatorial ports #3 and #11. The images acquired correspond to the two poloidal sections of the vessel, comprising both in-coming (forward view) and out-going (backward view) RE flight direction. In this work, the data acquired from the three CCD camera are processed in order to infer the pitch angle parameters.

3.5 RE characterisation

The synchrotron radiation is a powerful tool to estimate the most important RE parameters, namely the pitch angle θ and the energy in the different phases of the discharge.

Figure 3.4 is an example of the importance of the pitch angle estimation. It shows the dependence of the synchrotron emission spectra from the pitch angle parameter.

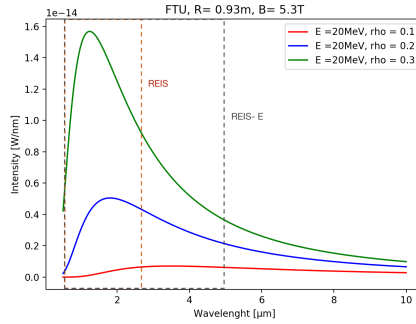


Figure 3.4 Synchrotron emission spectra at different energies and different pitch angle parameters [16]. The dashed lines show the spectral range of the REIS diagnostic and the upgrade version REIS-E diagnostic.

The *pitch angle* is defined as the angle between the particle velocity vector and the magnetic field

$$\theta = \frac{v_{\perp}}{v_{\parallel}} \quad (3.2)$$

where v_{\perp} is the velocity component perpendicular to the magnetic field and v_{\parallel} is the velocity component parallel to the magnetic field

field. Generally, synchrotron radiation spectra measurements, in a typical FTU runaway discharge, indicate RE energies up to 30MeV [64]. The synchrotron radiation is sensitive to a small part of the RE energy distribution function. By following the approach used in [67–69], the pitch angle value can be inferred from the synchrotron radiation divergence of the 2D camera images. The physics behind the synchrotron spot shape is determined by the cone of RE synchrotron radiation. The signal of the visible camera is dominated by the fastest electrons, creating a tight energy range. On the basis of this preliminary hypothesis, it is possible to deduce that the pitch angle θ is related to the observed elongation of the plasma torus. The full opening angle is approximately twice the RE pitch angle as:

$$\alpha = 2\theta + \frac{1}{\gamma} \approx 2\theta \quad (3.3)$$

where γ is the electron energy. It is possible to neglect the term $1/\gamma$ because it is an order of magnitude smaller than the inferred value of θ . Figure 3.5 illustrates the horizontal extension of the electron radiation. As it can be notice, the electron covers a circular orbit having radius equal to R_m . The camera detects the radiation only along the blue arc.

As a consequence of the toroidal curvature and of the finite angle α , the horizontal dimension is greater than the vertical dimension of the quantity:

$$\Delta r = R_m(1 - \cos\theta) \approx R_m\theta^2 \quad (3.4)$$

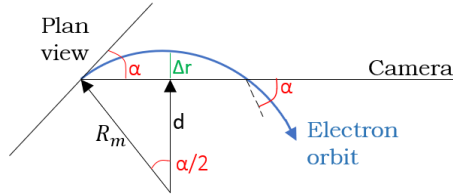


Figure 3.5 Schematic of the extension of the detected synchrotron radiation in the horizontal direction.

It is possible under certain circumstances to assume the detected radiation as having an elliptical shape. The ellipse can form islands or snakes [70], can be tilted by the safety factor of the machine [68, 71] or can form a crescent shape due to orbit effect [72].

The fitting to an horizontal ellipse is possible when the following condition is satisfied:

$$\theta \gg \frac{r_{beam}}{q(r)_{beam} R_m} \quad (3.5)$$

where $q(r)$ is the safety factor, R_m is the plasma axis major radius, and r_{beam} is the largest radius r , that determines the size of the beam. The condition 3.5 is satisfied in our case, since the pitch angle values span in the range [0.04 – 0.44], as we will see in Section 3.7. For instance, referring to the data of shot #39516, the computed value is

$$\frac{r_{beam}}{q(r)_{beam} R_m} = 0.0934$$

where r_{beam} is overestimated considering it equal to the plasma radius, $q(r)_{beam}$ is the mean value between the safety factor values on

the edge and on the axis, R_m is equal to $0.95m$. Based on the results obtained, it can be stated that the fitting to an ellipse is possible.

3.6 Architecture of the software platform

The image-processing procedure was designed using the software MATLAB. The target of the platform is to infer the pitch angle parameter from different images of FTU plasma discharges. Figure 3.6 illustrates a time sequence of visible images of the RE beam in FTU backward and forward view.

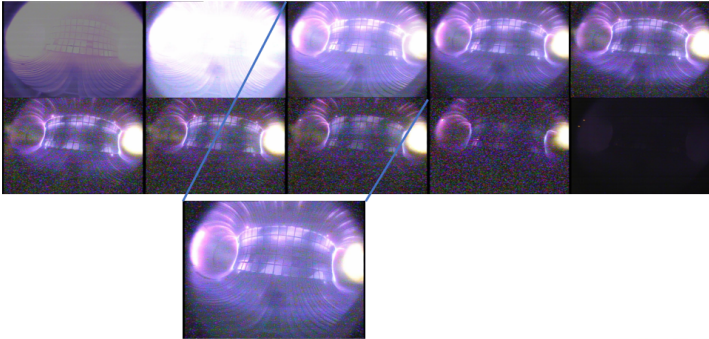


Figure 3.6 Time sequence of RE visible light images acquired in FTU during discharge #41738.

The main important steps of the algorithm are shown in the flow chart illustrated in Figure 3.7.

The synchrotron radiation images are imported in MATLAB as pixel matrices. Before the estimation procedure, the images are corrected by geometric effects due to the camera position inside the vessel. The pitch angle value can be inferred from the synchrotron image

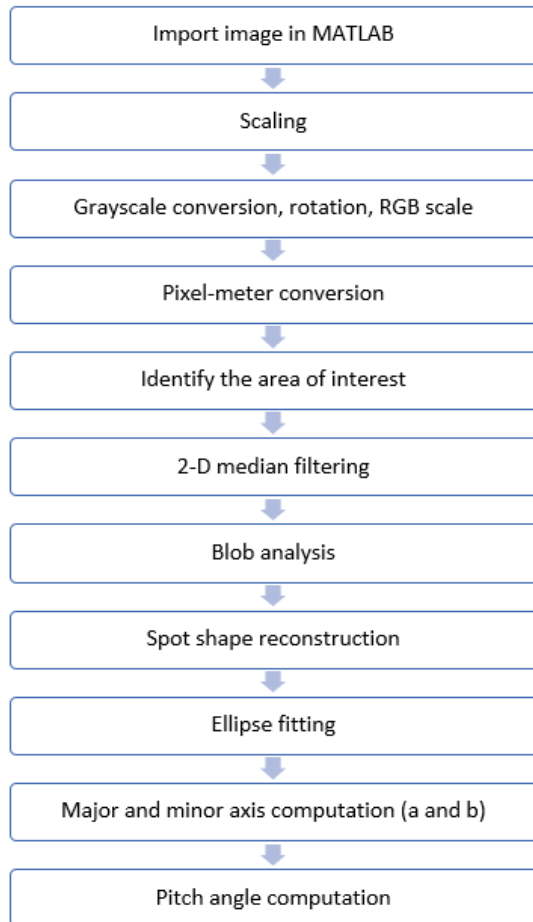


Figure 3.7 Flow chart of the MATLAB platform.

analysing the elongation of the elliptic shape of the RE beam. The visible energy of the bundle, shown in the images, is qualitative identified using the thresholding method with respect to the maximum intensity.

The images analysed are characterised by a significant problem: the spot of interest is cut. Consequently, we didn't know exactly the measures of the two ellipse axes. In this case all the standard fitting procedure for ellipse cannot be applied. The procedure followed consists of implementing the best ellipse reconstruction. In the initial phase of the analysis [48], the symmetrical part of the visible images was reconstructed. Progressively [49], the algorithm was improved starting from the minimum point of the spot corresponding to the largest width of the shape. The spot is cut in the upper part, due to the position of the camera. After identifying the area of interest, the missing part of the spot was reconstructed.

The last step was the ellipse fit of the RE beam image. The pitch angle found has the following analytical expression [67]:

$$\theta = \sqrt{\frac{(a - b)}{R_m}} \quad (3.6)$$

where a is the ellipse major axis, b is the minor one and R_m is the position of the magnetic axes.

3.7 Simulation results

The different steps of the algorithm are explained considering a particular image, for instance image 25 (corresponding to $t = 0.5s$), shot

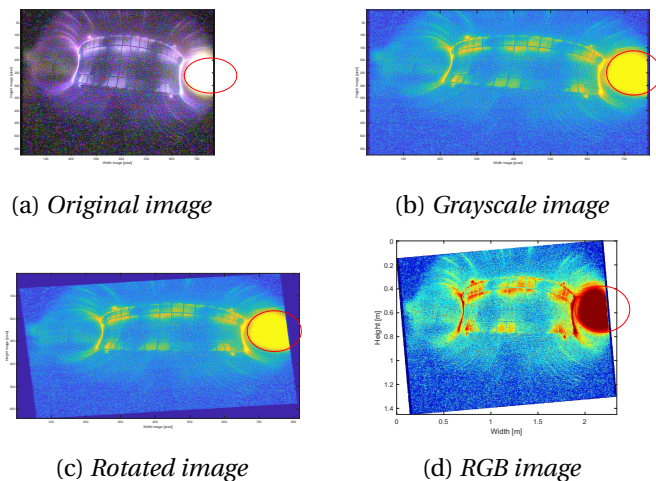


Figure 3.8 First steps of the image-processing algorithm.

#41738, FTU port 3.

The image is imported in MATLAB as pixel matrix, as shown in Figure 3.8a, where each pixel correspond to the brightness of each point of the image. In the first phase of the processing procedure, the image is suitably converted in grayscale values, see Figure 3.8b, rotated with respect to the equatorial plane, see Figure 3.8c and mapped in a RGB scale image, as shown in Figure 3.8d. The red circle in the illustrations of Figure 3.8 indicates the area of the synchrotron radiation spot.

Figure 3.8d shows the result of the pixel to meter conversion procedure. In this way the pixel coordinates of the image are converted in real-world coordinates, in order to obtain the measure of the geometrical shape using real-world units.

In the second part of the algorithm, the image is processed to identify the area of interest.

Figure 3.9 shows the visible energy of the beam identified using the thresholding method. The selected area, shown in Figure 3.10a, is processed using a 2-D median filtering. In order to obtain an homogeneous contour, each output pixel contains the median value in the 12×12 neighbourhood around the corresponding pixel in the input image.

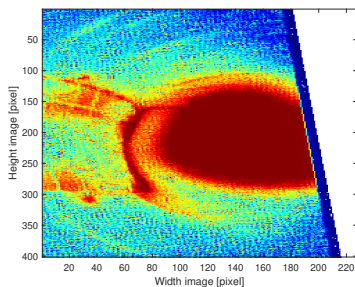
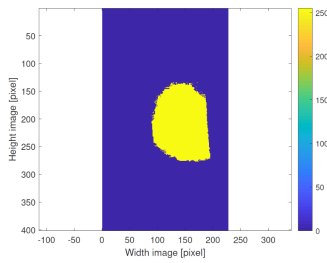


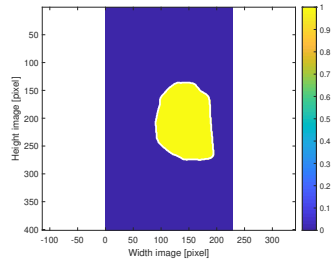
Figure 3.9 Zoom on the spot of the RE.

The filtered image is converted in binary form, see Figure 3.10b, in order to be processed using the Blob analysis technique, that allows to calculate the geometrical properties of the labeled region. Considering as reference point the minimum value of the spot that correspond to the largest shape width, the area of interest is reconstructed, as shown in Figure 3.10d. The missing part of the shape is reconstructed considering the symmetrical part respect to the retrieved area, like shown in Figure 3.10d.

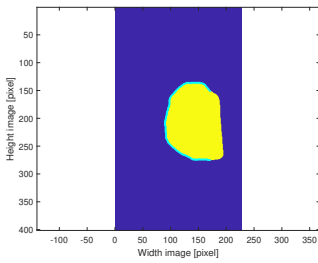
Following the reconstruction procedure, the Least Squares criterion is applied for the fitting procedure. Assuming the well know elliptical shape of the bundle, the best fit to a geometrical ellipse for the given set of points is done.



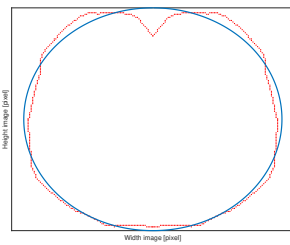
(a) *Focus on the synchrotron spot*



(b) *Binary filter spot*



(c) *Area of interest bounding*



(d) *Reconstructed ellipse*

Figure 3.10 Second part of the image-processing algorithm.

In Figure 3.11 are illustrated the axes of the fitted ellipse. From the major and minor axis values, the pitch angle can be inferred in the case under examination. The value obtained is $\theta = 0.3725$, characterised by an horizontal axis extension greater than the vertical axis extension, confirming the theoretical hypothesis.

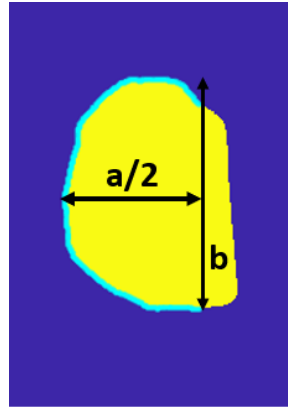


Figure 3.11 Axes of the fitted ellipse.

The procedure was automated for all the images of different shots of FTU port 3. Figure 3.12 shows the pitch angle trend over time, in the case of shot #39516, #41738, #41744.

From the analysis of the 2 – D beam elongation, it can be deduced that the runaway electrons that dominate the synchrotron image have a wide distribution of the pitch angle values spanning in the range $[0.04 - 0.44]$, values consistent with similar physical processes observed in other tokamaks [73].

3.8 Conclusion

Understanding the main rules that govern the RE behaviour is the key for the tokamak operations safety and security. RE synchrotron radiation is a powerful tool to investigate the RE physical behaviour. The visible images, acquired in FTU through a CCD camera, are analysed using an automatic software platform. From the image-processing procedure, the pitch angle values of the observed shape are inferred.

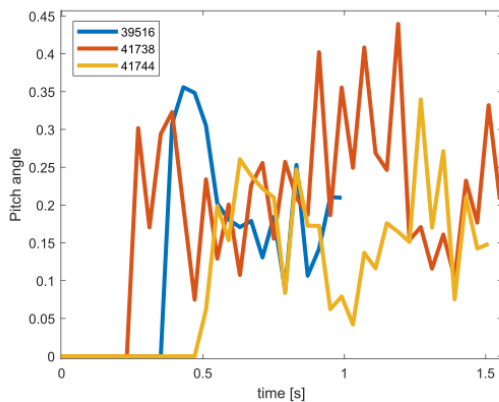


Figure 3.12 Graph of the pitch angle trend for different FTU discharges.

Such information, when combined with the analysis of synchrotron spectra, can provide a better assessment of the RE energy distribution function, leading to improved RE control strategies. In the next chapter, the diagnostic tool SOFT [20] is used to simulate the FTU synchrotron images. A comparison with the experimental spectra is done in parallel, in order to have more significant and consistent results.

Chapter 4

Simulation of Runaway Electrons synchrotron radiation in FTU

4.1 Introduction

The key to investigate and control runaway electrons (REs) dynamics is the development of *theoretical models*. In the tokamak history, different models and studies have been conducted. The synchrotron radiation was exploited, for the first time, as diagnostic tool for RE in [17]. The first models were based on the curvature radius or RE pitch angle estimation from the synchrotron data [17], while, more recently, the models also focused on RE distribution function and magnetic field geometry [71, 74].

For the FTU simulations, the *Synchrotron-detecting Orbit Follow-*

ing Toolkit (SOFT) [20] has been used. SOFT is a synthetic radiation diagnostic model, designed to model synchrotron radiation and bremsstrahlung emitted from RE in tokamaks. The highlights of the diagnostic is the use of a simplified emission model, namely the cone model, that allows to obtain good results maintaining low computational cost. In contrast to other simulation softwares, SOFT takes into account the geometric effects contribution, like the camera position and the magnetic field inhomogeneity [73].

4.2 Preliminary studies

The aim the research conducted is to simulate experimental synchrotron data, exploiting a continuous comparison between images and spectra simulation results.

4.2.1 Data selection

For this reason, the first step was to choose the data that can provide more information from images and spectra. The data from a shot (#43651 from the last experimental campaign of FTU (2019)) have been selected. It has been chosen the shot for which good synchrotron images and spectral data were available simultaneously. Figure 4.1 shows a time sequence of RE synchrotron images in the case of the above mentioned shot (#43651).

Table 4.1 summarises the main characteristics of shot #43651.

The images are acquired through the visible CCD camera installed in FTU port 3, instead the spectra data are acquired through the REIS-E spectrometers. REIS-E is an upgrade version of the REIS, used in the

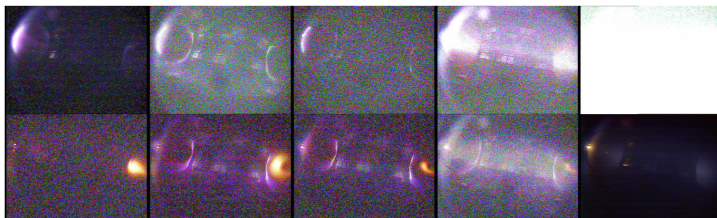


Figure 4.1 Time sequence of RE synchrotron images in the case of shot #43651.

Parameter	Value	Base unit
Toroidal Magnetic Field (B)	5.3	T
Plasma Current (I_p)	0.35	MA
Electron density (n_e)	0.13E20	m^{-3}
Electron Temperature (Te)	2.0	keV
RE generation	YES	//
Pellets (t)	0.3 -0.38-0.38	s

Table 4.1 Main important parameters of pulse #43651 at time 0.25s.

last FTU campaign. In the REIS system [16, 64], described in Chapter 3, the spectra extension reached $2.5\mu m$, instead the REIS-E spectra extension reaches $5\mu m$.

The data corresponding to 700ms has been analysed. Figure 4.2 and Figure 4.3 show an example of experimental data.

4.2.2 Time setting images port 3

The images acquired in FTU are collected in different folders and numerated from 0 to the total number of frames of the shot. In order

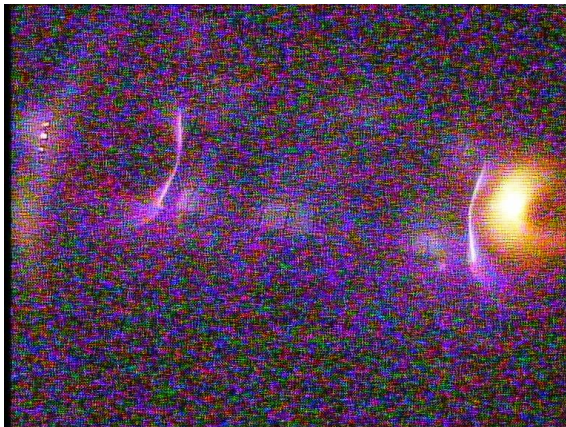


Figure 4.2 Original FTU image at 700ms.

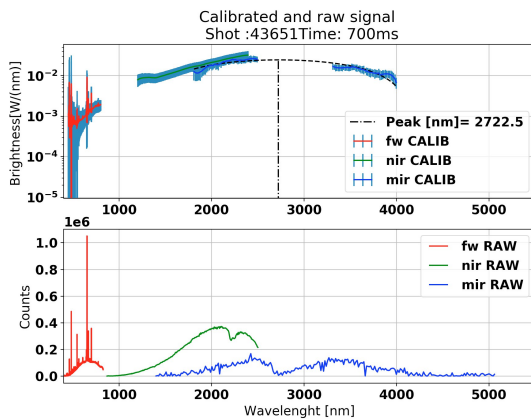


Figure 4.3 Experimental synchrotron spectra at 700ms.

to associate the number of frame to the corresponding acquisition time the camera setting must be evaluated. The camera started the images acquisition in correspondence to the start trigger of the shot, using a 25 Hz frame rate (temporal window = 40 ms). The exposure time is set automatically in the camera, in other words, it is variable and changes in function of the detected luminosity. This particular setting allows to avoid image saturation. The frame repetition is fixed, but the shutter aperture, inside this window, is changed in function of the detected amount of light. For the camera used, the aperture time ranges from $1/10000\text{ s}$ to a maximum of $1/50\text{ s}$, in which is open for the overall acquisition. The time of each acquired frame is associated to half of the acquisition interval, as follows:

$$time = (frame * temporal_window) + 20ms \quad (4.1)$$

where *frame* is the number of frame (starting from 0), *temporal_window* is the acquisition window and 20 ms is added in order to select the central part of the window. In our specific case, we found that the frame 17 is associated to 700 ms .

4.2.3 Intensity light variation

In order to validate the hypothesis and check the association between time acquisition and number of frame, a study of the integral of the *intensity light variation in function of time* has been done. As regards the images, different analysis starting from a single pixel variation over time to the overall synchrotron spot has been performed. Figure 4.4 illustrates an example of selected area in the case of shot #43651.

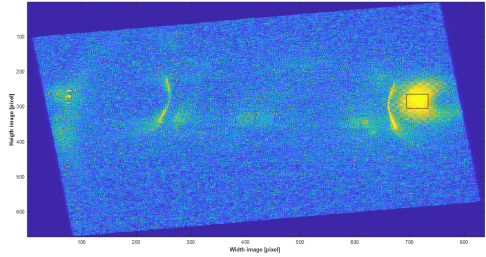
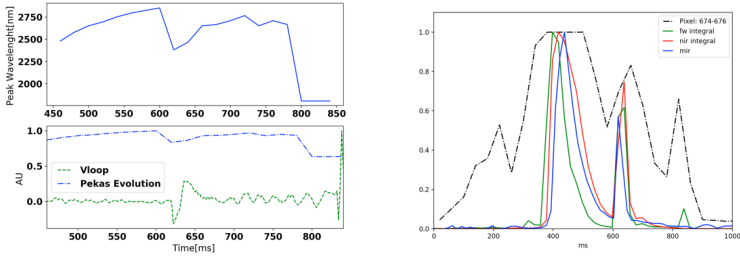


Figure 4.4 Selected image area.



(a) Peaks and v_{loop} data

(b) Pixel intensity time evolution

Figure 4.5 Light intensity variation analysis.

The next step was to compare the pixels values found with the peaks evaluation of the spectra and the v_{loop} signal, shown in Figure 4.5a. Figure 4.5b shows the pixel intensity time evolution, in the case of images and spectra analysis.

The signal of the camera is different from the fw integral because of the different exposure duration at different times. Calculating the ratio of the the pixels intensity time evolution to the fw spectrometer intensity time evolution, the graph in Figure 4.6 has been obtained.

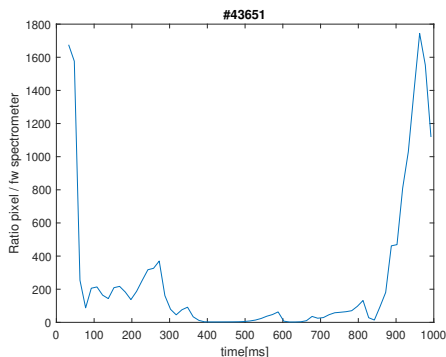


Figure 4.6 Ratio pixels images variation/fw spectrometer variation.

As can be seen, the variation of the ratio in the time interval around 700 ms is negligible and therefore the time association selected above for the time frames of the camera images can be considered correct.

4.2.4 Plasma parameters

Chosen the time of interest (700ms), it is possible to fix *plasma parameters* necessary to run the SOFT simulations. FTU is equipped with different diagnostic systems designed to perform the physical quantities measurements (a detailed description of diagnostics installed in FTU ports can be found in [15]). The data are acquired in the FTU database and stored in channels. A convenient way to obtain information about the shot is to use the software *shox* [75]. Time traces of some important plasma parameters, for shot #43651, are shown in Figure 4.7.

In the next section 4.3 we will see in the detail the parameters used in our specific case.

70 Simulation of Runaway Electrons synchrotron radiation in FTU

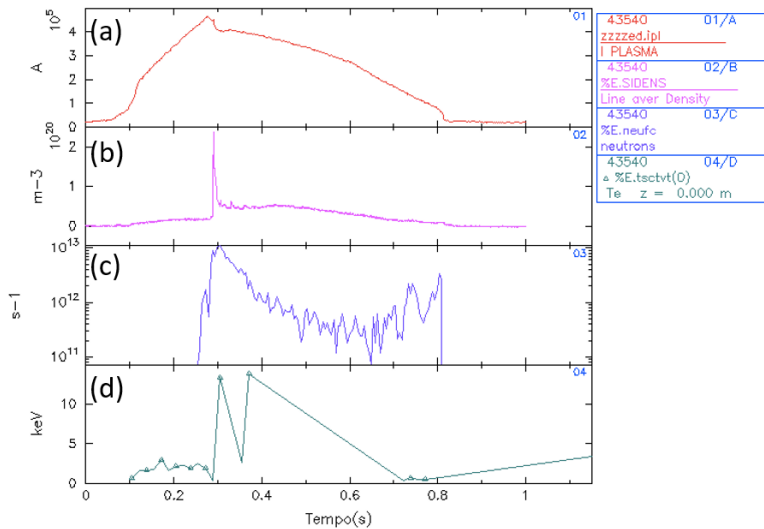


Figure 4.7 Plasma parameters time traces for shot #43651. (a) Total plasma current (b) Density in the plasma centre ($R_m = 0.935m$) (c) Total neutron emission (d) Temperature in the plasma centre ($R_m = 0.935m$).

4.3 SOFT parameters selection

The second version of SOFT, called SOFT2 (or SOFTv2), that is an upgrade of the first version containing several improvements, has been used. The SOFT diagnostic is based on configuration script, referred as *pi file*. The pi file includes a list of options and modules that can be configured. More details can be found in the online guide [76]. Below, we will see in detail how the different parameters have been chosen.

4.3.1 Radiation diagnostic

The main target of the SOFT tool is the radiation diagnostic estimation. The module used is the *@Radiation tool*, that evaluates the different form of the radiation diagnostic integral [20], expressed in Eq. (4.2), in order to calculate radiation images, spectra and Green's functions:

$$I = \iiint \Theta \left(\frac{\mathbf{r}}{r} \right) \frac{\mathbf{r} \cdot \hat{\mathbf{n}}}{r^3} \frac{dI(\mathbf{x}, \mathbf{p}, \mathbf{r})}{d\Omega} f(\mathbf{x}, \mathbf{p}) d\mathbf{p} dV dA \quad (4.2)$$

where I is the general radiation quantity (for example radiated power, spectral power or number of photons), Θ indicates the field-of-view step function, $\mathbf{r} = \mathbf{x}_0 - \mathbf{x}$ is the vector from the point of space \mathbf{x} where radiation begins to the detector (\mathbf{x}_0), $\hat{\mathbf{n}}$ is the normal of the detector surface, $\frac{dI}{d\Omega}$ describes the angular distribution of radiation emitted and $f(\mathbf{x}, \mathbf{p})$ is the electron distribution function. The integration is calculated considering all the momentum space (as denoted by the differential $d\mathbf{p}$), real space (indicated by the volume dV) and detector surface (denoted by dA). Starting from the integral 4.2,

it was developed in [73] a theory to simplify the calculations. The set of coordinates were transformed in guiding-center coordinates, that are more suitable for runaway orbits integration. Based on this transformation, the radiation diagnostic integral has the following form:

$$I = \iiint \Theta\left(\frac{\mathbf{r}}{r}\right) \frac{\mathbf{r} \cdot \hat{\mathbf{n}}}{r^3} \frac{dI(\mathbf{X}, \mathbf{p}, \mathbf{r})}{d\Omega} f(\rho, p_{\parallel}, p_{\perp}) J \underbrace{dp_{\parallel} dp_{\perp} d\zeta}_{d\mathbf{p}} \underbrace{d\rho d\tau d\phi dA}_{d\mathbf{X}} \quad (4.3)$$

where \mathbf{X} is the guiding-center position, ρ is the maximum major radius reached by a guiding-center orbit, p_{\parallel}, p_{\perp} are the particle momenta components parallel and perpendicular to the magnetic field, ζ denotes the gyro angle, τ indicates the time coordinate along guiding-center trajectory and ϕ is the toroidal angle. In the case under examination, the *@Radiation tool* has been set with the cone model parameter (for more details on the simplified cone model see [73]) and image and green have been selected as output. In addition, it is possible to set a resolution parameter (*ntoroidal*) defining the number of toroidal sections used in the radiation diagnostic integral. In the following the parameters chosen:

```
@RadiationModel cone (cone) {
    emission = synchrotron;
}
```

```
@Radiation rad {
    detector = det;
```

```
    ntoroidal    = 7000;  
    model       = cone;  
    output      = image, green;  
}
```

One important radiation sub-model is the *@Detector*. The parameters have been fixed considering the different localisation of the visible camera and spectrometers.

4.3.2 Detector

Let's see in detail the parameters set in the *@Detector module*. In FTU port 3 was installed the camera IK-M51H [77]. The first parameters are the detector *position* and *direction*, that represent respectively the position relative to the point of symmetry of the tokamak and the viewing direction. As reference the Figure 4.8 illustrates the coordinate system used in SOFT.

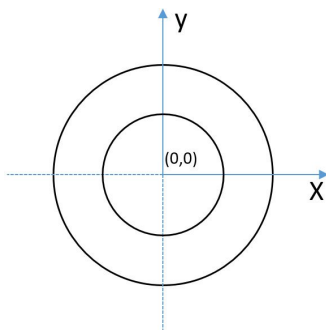


Figure 4.8 Coordinate system convention.

74 Simulation of Runaway Electrons synchrotron radiation in FTU

The relative camera position has the following coordinates:

$$x = 0m$$

$$y = 0.935m + 0.330m = 1.265m$$

$$z = -0.165m$$

where $0.935m$ is the plasma major radius, $0.330m$ is distance from the plasma center and $0.165m$ is the position of the camera below to the equatorial plane. The direction is set along the y axis.

Another parameter is the *aperture*. In SOFT the detector is approximated as a square, which side length correspond to the size of detector aperture (more details can be found in the camera data sheet [77]).

The *vision_angle* parameter is defined as half of the opening angle of the field of view.

The *spectrum* parameter allows to define the detector spectral range features. The first two numbers indicate the lower and upper limits of the spectral bound, the third number the resolution, that is the number of points inside the interval. In the case of synchrotron emission model, the spectrum boundaries are expressed in units of meters. Values in the visible range of the spectrum have been chosen.

Finally, it is possible to specify the camera *rotation* respect to the horizontal plane. In the case under study, the camera installed on port 3 has a 7.5° inclination respect to the equatorial plane. The angle must be expressed in radians (the original value is converted and multiply by 2 because the trigonometric function in the code are normalised at $180^\circ/\pi$). In the following are summarise the @Detector parameters chosen:

```
@Detector det {  
    position      = 0, -1.265, -0.165; # [m]  
    direction     = 0, 1, 0;  
    aperture      = 0.017; # [m]  
    vision_angle  = 0.89 image; # [rad]  
    spectrum      = 400e-9, 650e-9, 10; # [m]  
    roll          = 0.262; # [m]  
}
```

Similar reasoning was conducted in the case of REIS spectrometers, located in the FTU port 6.

4.3.3 Magnetic field

The module *@MagneticField* allows to set the magnetic field features and the domain (walls) to use. Two options are available: analytical and numerical. The analytical is the easiest and fastest, in which the magnetic field structure is composed of circular surfaces. Instead the numerical option allows more advanced application, giving the possibility to put as input a 2D numerical magnetic field. In the case under study, the analytical option has been used as starting point. The toroidal magnetic field is inferred from the experimental data acquired by the FTU diagnostic, in particular channel %E.BTOR of the shox software shows the magnetic behaviour over time (Figure 4.9).

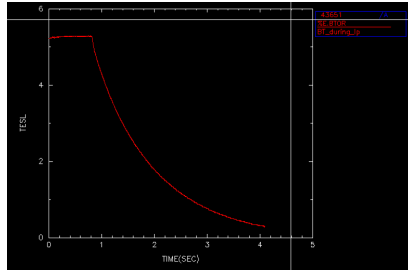


Figure 4.9 Shox: toroidal magnetic field B_0 . It can be, approximately, considered constant in the range of interest 0 – 0.9s.

Safety factor

Considering the magnetic field, the *safety factor* q affects the synchrotron spot. It is defined as the ratio of toroidal to poloidal turns for a magnetic field surface and gives a measure of how twisted is the magnetic field. In the `@MagneticField` module it is possible to specify the safety factor parameter and its radial dependence. It has been chosen a quadratic functional form:

$$q(a) = q_{a1} a^2 + q_{a2}$$

where a is the normalised minor radius and q_{a1} and q_{a2} are constant. Based on the data of the shox channel %E.EQLQVR, shown in Figure 4.10, the constant values are inferred. In particular,

$$q_{a2} = q_0$$

$$q_{a1} = q_{psi} - q_0$$

where q_0 is the on axis value, q_{psi} is the value on the plasma edge.

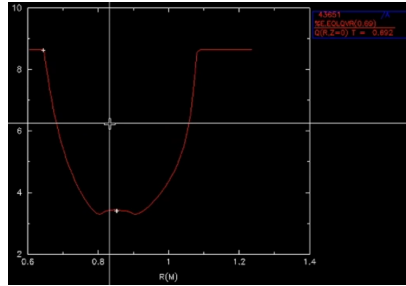


Figure 4.10 Shox: safety factor.

Other options set in the module are the tokamak major and minor radii (see Table 1.1) and the orientation of the toroidal component (clock-wise direction in this case). The *@MagneticField* parameters chosen are the following:

```
@MagneticField mf ( analytical ) {
    B0      = 5.263423420301871; # (T)
    Rm      = 0.935; # (m)
    rminor  = 0.3; # (m)

    # Safety-factor
    qtype   = quadratic;
    qa1     = 5.341455358611038;
    qa2     = 3.3278176278126135;

    sigmaB = cw;
}
```

4.3.4 Distribution function

The distribution function, defined in Chapter 1, can be set in the module *@DistributionFunction*. Different types of distribution functions can be chosen. The target is to find a distribution function that allows to obtain the best matching between experimental data and simulations. The simulations has been performed using three type of distribution functions: monoenergetic, avalanche and exponential pitch distribution.

In the first case, the RE have a mono-energetic and mono-pitch angle distribution. The parameters of this type of distribution are set in the phase space grid (it will be better described in Subsection 4.3.5).

Assuming a spatially homogeneous plasma with constant electric field and runaway generation dominated by the avalanche mechanism, the avalanche distribution function can be expressed in the following form [78]:

$$f(p, \xi) = \frac{A(p)}{2\pi m_e c \gamma_0 p^2} \frac{\exp[-\gamma/\gamma_0 - A(p)(1 + \xi)]}{1 - \exp[-2A(p)]} \quad (4.4)$$

with

$$A(p) = \frac{\hat{E} + 1}{Z_{eff} + 1} \gamma$$

$$\gamma_0 = \log \Lambda \sqrt{Z_{eff} + 5}$$

where p is the particle momentum normalised to the electron rest mass ($m_e c$, with c speed of light in vacuum), $\xi = \cos \theta_p$ denotes the particle pitch angle with respect to the magnetic field ($\gamma = \sqrt{1 + p^2}$), \hat{E} is the electric field strength respect to the threshold electric field, $\log \Lambda$ is the Coulomb logarithm and Z_{eff} is the plasma effective

charge.

Based on this assumption, three different parameters have been set in the SOFT simulations: the electric field strength (E_{hat}), the Coulomb logarithm ($\log\Lambda$) and the effective plasma charge (Z_{eff}). The electric field strength is equal to:

$$\hat{E} = \frac{v_{loop}}{2 * \pi * R_m} E_c \quad (4.5)$$

where v_{loop} is the loop voltage, R_m is the plasma major radius and E_c is the critical electric field. The critical electric field E_c depends on quantities that are function of time:

$$E_c = \frac{density e^3 \log\Lambda}{4\pi\epsilon_0^2 m_e c^2} \quad (4.6)$$

where $density$ denotes the particles density, e is the Coulomb charge and ϵ_0 the dielectric constant. Figure 4.11 shows the time evolution of v_{loop} and particle density in the case of shot #43651.

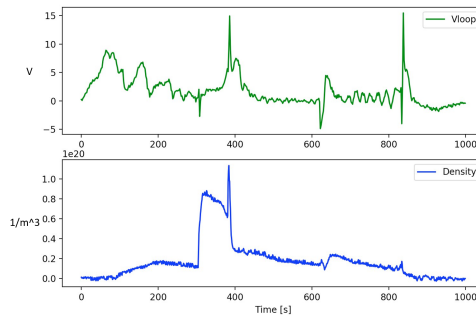


Figure 4.11 Loop voltage and density time traces in the case of shot #43651.

80 Simulation of Runaway Electrons synchrotron radiation in FTU

Based on the temperature and density values of #43651 (Table 4.1), the value of the Coulomb logarithm for electron ions collision is fixed at 17 for all the simulations [4].

Taking into account the experimental errors, Z_{eff} has been assumed to have a value of about 6, as confirmed by the time trace in Figure 4.12, acquired by the diagnostic system.

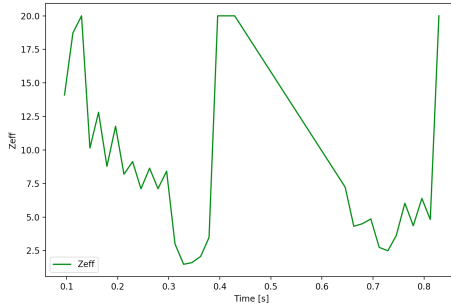


Figure 4.12 Plasma effective charge Z_{eff} time trace for shot #43651.

The parameters selection is summarise in the following:

```
@DistributionFunction analytical_avalanche (avalanche) {  
    EHat = 0.016;  
    lnLambda = 17;  
    Zeff      = 6;  
}
```

The third type of distribution function used in the simulations is the pitch distribution function, that is the pitch part of the analytical avalanche. It can be expressed as the cosine of the pitch angle:

$$f(\xi) = \exp(C\xi) \quad (4.7)$$

where C is the input parameter and $\xi = \cos\theta$. In the case under examination, the best results have been found using an exponential pitch distribution. The C parameter was set equal to 200, corresponding to a dominant pitch angle equal to $\theta = 0.259rad$.

The pi file in that case was set in the following way:

```
distribution_function = ourDistribution ;

@DistributionFunction ourDistribution (pitch) {
    C=200;
}
```

In addition, SOFT allows to set the radial profile distribution. When not specified, it will be set uniform (function = 1) as default. In Section 4.4 an extra tool to find the radial profile from the data will be shown.

4.3.5 Phase space grid

The module *@ParticleGenerator* allows to set the type of particles (default value correspond to the electron charge) to simulate and the limit of the phase space in which consider the particles (initial position, pitch angle and energy). Different simulations have been performed in order to test the influence of the single parameters in the synchrotron spot. The following parameters have been used to obtain image 4.13b:

```
@ParticleGenerator PGen {
    a      = 0, 0.9, 60;
    p      = 20, 20, 1;
```

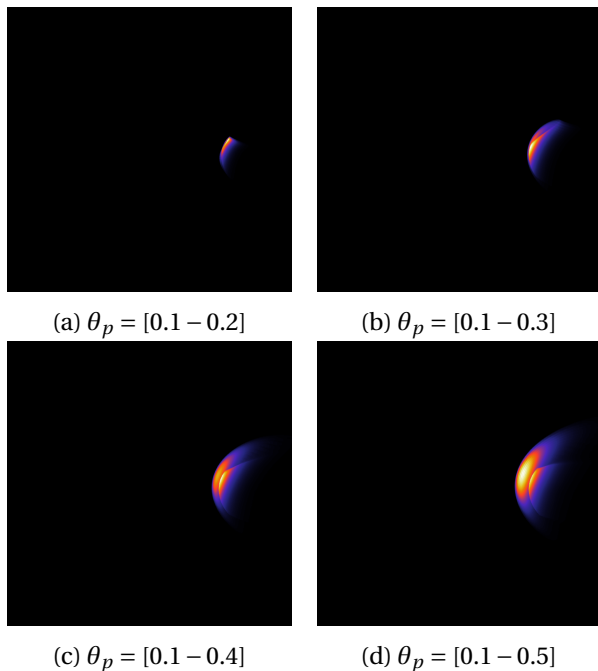


Figure 4.13 Pitch angle variation analysis.

```
thetap = 0.1, 0.3, 40;  
}
```

Figure 4.13 illustrates an example of pitch angle studies performed. It is possible to note that increasing the pitch angle values, the vertical extent increases. At a threshold value two different spots are simulated moving away from each other.

4.4 Radial profile of runaway electrons

RE inside tokamaks plasma are widely distributed in the phase-space.

4.4.1 Radial distribution

The first simulations have been performed considering an *uniform radial distribution*. The SOFT toolkit is equipped with an additional software named *softplot*, that allows to test directly the different radial distribution effect in the synchrotron spot. By comparing the simulated images with the experimental image 4.2, it has been found a good shape agreement using a *Gaussian radial profile*

$$\exp(-((x - 0.4)/0.2) * * 2)$$

as shown in Figure 4.14.

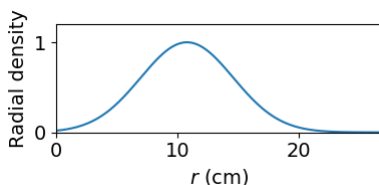


Figure 4.14 Gaussian radial profile.

Figure 4.15 shows a comparison between synchrotron images obtained applying the uniform radial profile (4.15a) and the Gaussian radial profile (4.15b) aforementioned.

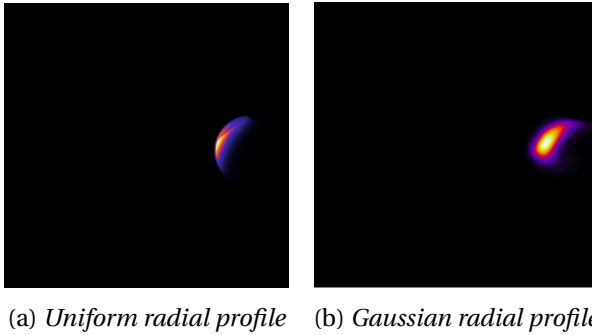


Figure 4.15 Comparison of synchrotron images using different radial profile distribution.

4.4.2 Image inversion procedure

Finding more precise radial distribution is essential to obtain the best synchrotron modelling. For this reason, a new approach has been followed. The image inversion procedure is based on *Tikhonov regularization algorithm*. This technique finds the best radial profile which must be applied to the simulated images in order to match the real ones. It is a very efficient method used to estimate the parameters comparing the experimental image (Figure 4.16(a)) with the simulation result (Figure 4.16(c)). Figure 4.16 shows a preliminary result of the inversion procedure. The radial distribution (Figure 4.16(b)) is obtained from the comparison of the two data.

After finding the reconstructed radial profile, the data are fitted using a Gaussian profile, as shown in Figure 4.17. The parameters found are applied to the experimental image by using the softplot tool.

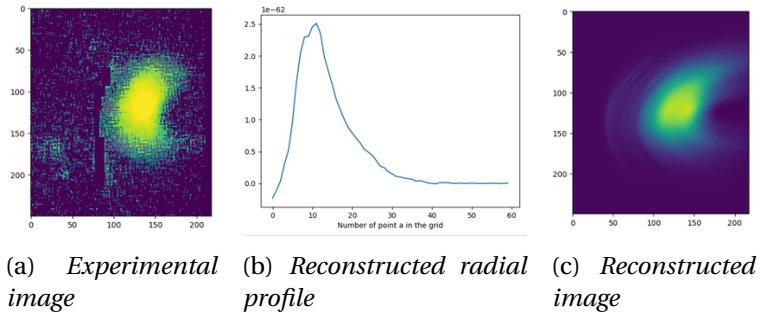


Figure 4.16 Output results of the image inversion procedure.

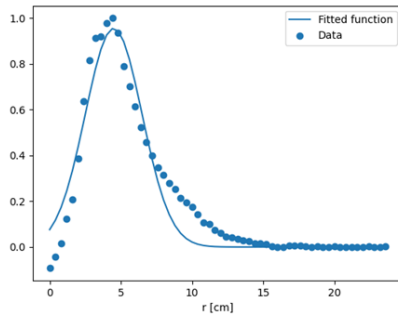


Figure 4.17 Radial profile fitting.

4.5 Results

Different simulations and combinations of phase-space parameters have been performed. The comparison between spectra simulation and experimental spectra data gives useful information in term of energy constraint. For each spectra simulation a constant minimising the root mean square is found and the lowest value is chosen.

Based on these studies, parallel analysis has been conducted for the images. The best parameters allowing to increase the similarity between experimental and simulation data are found applying an exponential monoenergetic distribution having:

$$p = 24.5, \text{thetap} = 0.3$$

Figure 4.18 illustrates the experimental data compared with the simulated experimental spectra. The blue line indicates the experimental error on data. It can be seen that there is a good matching.

Figure 4.19 shows a comparison between the experimental image and the image obtained with SOFT. The phase-space parameters are chosen according to the spectra results.

The pitch angle values used are consistent with the previous study performed using the platform described in Chapter 3, shown in Section 3.7. In particular, the radial distribution of the RE is the fitted Gaussian found in Section 4.4. It is possible to confirm a good matching between simulation and experimental data.

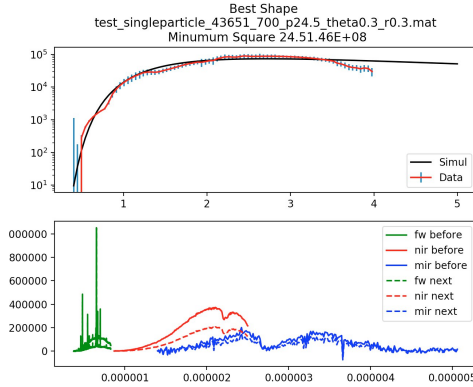


Figure 4.18 Best spectra results at 700ms.

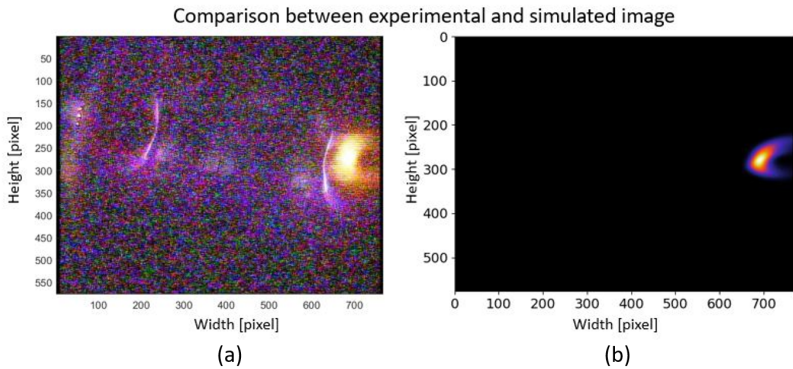


Figure 4.19 Best synchrotron images results at 700ms, #43651. (a) Experimental image. (c) SOFT simulation using a Gaussian radial profile.

4.6 Conclusion

Synchrotron radiation is a powerful tool for understanding RE dynamics, but a complete model is necessary to obtain a correct simulation procedure. The software SOFT was chosen to simulate the synchrotron images and spectra by solving the guiding-center RE equations of motion and calculating their radiation emission. A good match has been found between the estimates of the RE pitch angle and energy derived from image analysis (this thesis) and spectral analysis, both supported by SOFT simulations.

The nuclear fusion field is continuously changing and innovating. In the next chapter, a new optical remote sensing technique is investigated. The technique presented can be the basis for new fusion plasma diagnostics.

Chapter 5

Remote recovery of audio signals from videos of optical speckle patterns

5.1 Introduction

Optical remote sensing is an innovative technique, that allows to analyse noninvasively the environment, even at long distances between probe and probed objects. In the research performed [79], a comparative analysis of recovery algorithms of audio signals from the silent videos of the optical *speckle patterns* movement [80] was carried out. Applications of optical remote sensing covers a wide range of disciplines. The techniques analysed can be a basis in future plasma physics applications.

5.2 Experimental setup

The setup proposed in [81, 82] was implemented, but, in this case, a *diode laser* was used. Diode laser are widespread in sensing applications, because they are cheap, efficient in terms of energy and cover an extensive range of wavelengths. Figure 5.1 (a) illustrates the experimental setup.

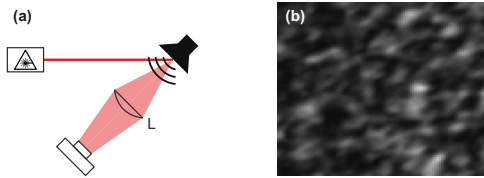


Figure 5.1 (a) Experimental setup: A collimated laser beam shines onto a white paper glued to the membrane of a loudspeaker. The paper surface roughness generates a speckle pattern that is imaged by lens L onto the sensor of a CMOS camera. (b) Example of a speckle image recorded by the camera.

The diode laser (Thorlabs HL6750MG, $\lambda = 685nm$) was driven by a Thorlabs ITC4001 controller. The light generated was collimated, through an iris (having $\sim 1mm$ diameter), at an angle of 40° onto the membrane of a loudspeaker (Logitech X-210 subwoofer). The speaker membrane was covered with a white paper in order to prevent the light absorption by the black surface of the speaker membrane. The speckle patterns, that originates from the roughness of the paper by a lens (focal distance $f = 100mm$), were acquired through the sensor of an 8-bit CMOS camera (IDS UI-1222LE-M, pixel size $6\mu m$). Figure 5.1 (b) shows an example of optical speckle pattern.

The dynamical variations of the speckle pattern when a sound was played by the speaker was recorded by the camera, running in video mode. The signals acquired had an high-frequency, as a consequence an high video frame rate was necessary. For instance, at 800 frames per seconds (fps), it is possible to recover audio frequencies of up to 400Hz. Two different type of audio signals was successful recovered: sinusoidal with frequencies between 60 Hz and 140 Hz and a song with a predominance of bass frequencies (Another One Bites the Dust by Queen). Some examples of acquired videos and recovered audio signals can be found here.

5.3 Recovery methods and performance measures

The target of the work is to perform a comparative study of six different algorithms for the recovery of the audio signals from the silent videos.

5.3.1 Methods

Before describing each method, the basic notation is defined: $I_i[n]$ is the intensity of the i -th pixel in frame n and $x[n] = x(nT_s)$ is the sampling of the audio signal $x(t)$ emitted by the speaker, with T_s being the sampling time. $y[n]$ indicates the recovered signal at time nT_s , which depends on pixel intensities (that are function of the audio signal). Assuming to neglect constant terms, delays and applying a linear approximation, the intensity of the i -th pixel in

frame n is defined:

$$I_i[n] = f_i(x[n]) + \sigma_i \epsilon_i[n] \approx \alpha_i x[n] + \sigma_i \epsilon_i[n]. \quad (5.1)$$

where α_i is a constant in time that can depend on the pixel and the signals $\epsilon_i[n]$ account for noise and intensity discretization; we assume they are uncorrelated white noise with unity variance. σ_i is the strength of the noise that can also depend on the pixel.

5.3.2 Differential processing scheme (DIF)

This method was proposed in the literature [81], it is based on a proportionality between the perturbation to be measured and the speckle pattern variations. The recovered signal is computed from the difference, pixel-to-pixel, between two consecutive frames: $y[n] = \sum_i |I_i[n] - I_i[n-1]|$. If Eq. (5.1) holds, the recovered signal is

$$y[n] = \sum_i |\alpha_i (x[n] - x[n-1]) + \sigma_i (\epsilon_i[n] - \epsilon_i[n-1])| \quad (5.2)$$

Since $y[n]$ does not vary linearly with $x[n]$, harmonic generation in the recovered signal due to the nonlinearity of the reconstruction occurs.

5.3.3 Mean intensity (MI)

A simple method is based on the mean intensity calculation of each video frame n , $y[n] = \frac{1}{N} \sum_i I_i[n]$, where N is the pixels number. If

Eq. (5.1) holds:

$$y[n] = \left(\sum_i \frac{\alpha_i}{N} \right) x[n] + \frac{1}{N} \sum_i \sigma_i \epsilon_i[n] \quad (5.3)$$

Therefore, $y[n]$ varies linearly with $x[n]$ but, considering that the α_i values are likely positive or negative, the sum $(\sum_i \frac{\alpha_i}{N})$ will likely be small and the signal, $x[n]$, will likely be hidden by the noise.

5.3.4 1-pixel method (1 PIX)

This algorithm is based on the selection of one single pixel r . The pixel intensity is used to reconstruct the signal $y[n] = I_r[n]$. The pixel chosen is the one that maximise the signal $I_r[n]$ variance. If Eq. (5.1) holds:

$$y[n] = \alpha_r x[n] + \sigma_r \epsilon_r[n] \quad (5.4)$$

Supposing that the noise strengths are all the same ($\sigma_i = \sigma$), the pixel with the largest intensity variance will maximise the signal to noise ratio (SNR).

5.3.5 Cross-Correlation (CC)

The Cross-Correlation method in a new algorithm proposed, based on the cross-correlation between the time series of the intensity of a reference pixel and the time series of the intensities of all other pixels. A reference pixel, r , is selected and the Pearson correlation, ρ , is computed between the intensity of each pixel, i , and the intensity of the reference pixel r : $C_i = \rho(I_i[n], I_r[n])$. If Eq. (5.1) holds and

supposing to neglect the noise, then

$$C_i = \text{sign}(\alpha_i \alpha_r) \tag{5.5}$$

This property is exploited to find the signs of the coefficients β_i in a weighted mean intensity, used to reconstruct the signal:

$$y[n] = \sum_i \beta_i I_i[n] \tag{5.6}$$

The weights are opportunely chosen such that they maximise the SNR. Supposing $\sigma_i = \sigma$ and using Eq. (5.1) the recovered signal is equal to:

$$y[n] = \left(\sum_i \beta_i \alpha_i \right) x[n] + \sigma \sum_i \beta_i \epsilon_i[n]. \tag{5.7}$$

$\text{SNR} \propto (\sum_i \beta_i \alpha_i) / \sqrt{\sum_i \beta_i^2}$ if the noise signals $\epsilon_i[n]$ are uncorrelated. Consequently, SNR will be maximised choosing the weights such that $\beta_i \propto \alpha_i$.

The Root Mean Square (RMS) of the signal $I_i[n]$ (L is the number of frame) is exploited to estimate α_i . By using the linear approximation, the following expression is obtained $\text{RMS}_i = \sqrt{P^2 \alpha_i^2 + \sigma^2}$, where P is the RMS power of the signal $x[n]$. Based on that, it follows $|\alpha_i| \propto \sqrt{\text{RMS}_i^2 - \sigma^2}$. Hypothesising that values of α_i are small enough to be neglected, $\min_i (\text{RMS}_i)$ is an estimation of the noise strength, and consequently, $|\alpha_i| \propto \sqrt{\text{RMS}_i^2 - \min_i^2 (\text{RMS}_i)}$. SNR will be maximised if the weights are $\beta_i \propto \alpha_i$, hence $|\beta_i| = \sqrt{\text{RMS}_i^2 - \min_i^2 (\text{RMS}_i)}$. The

correlation sign C_i is used to set the sign of β_i such that

$$\beta_i = \text{sign}(C_i) |\beta_i| = \text{sign}(C_i) \sqrt{\text{RMS}_i^2 - \min_i^2(\text{RMS}_i)}. \quad (5.8)$$

Combining Eq. (5.5), $\beta_i = \text{sign}(\alpha_i \alpha_r) |\beta_i|$ and Eq. (5.7), the following expression for the recovered signal is found:

$$y[n] = \text{sign}(\alpha_r) \left(\sum_i |\alpha_i \beta_i| \right) x[n] + \sum_i \text{sign}(\alpha_i \alpha_r) |\beta_i| \sigma_i \epsilon_i[n], \quad (5.9)$$

It is important to note that using the weights defined in Eq. (5.8) all the terms in the sum that multiplies $x[n]$ are positive. In order to obtain good results, a reference pixel with high RMS must be chosen.

5.3.6 Machine learning method (ML)

This technique uses the algorithm IsoMap [83] for dimensionality reduction, that allows to reconstruct time-varying features in a low-dimensional space. Each frame n is modelised as a point in a N -dimensional space whose coordinates are the values of the N pixels, $\{I_1[n] \dots I_N[n]\}$. The recorded video composed of L frames is represented by a sequence of L points in this high dimensional space. It is possible to locate the points in a low dimensional manifold because the pixels depend on few variables, like the position and velocity of the loudspeaker membrane. The IsoMap algorithm is used to find the coordinate of each frame in a low dimensional manifold. The algorithm receives as input each frame coordinate and calculates the distance between any two frames using the Euclidean pixel-to-pixel

distance. The audio signal can be recovered from the trajectory in the reduced space.

5.3.7 MIT method

The method, proposed by MIT researchers [84], allows to extract sound from videos of minute vibrations. The video scene must to be illuminated, because the setup is not based on laser-generated speckle, like in the setup presented in this work. The algorithm is based on the complex steerable pyramid [85, 86]. The motion of each pixel is analysed and a weighted average is performed for each scales and directions. In the next step all the directions and scales are synchronised respect to a chosen reference and added together in order to obtain the recovered signal.

5.3.8 Performance measures

Two different methods were used to compare the performance of the algorithms: the Signal-to-Noise and Distortion ratio (SINAD) [87] for the sinusoidal audio signals and the Pearson cross-correlation coefficient for the song. The SINAD measures (in dB) the ratio between the power of the signal and the rest of the power that corresponds to noise and distortion, $SINAD = P_{signal} / P_{nd}$.

In the Fast Fourier Transform (FFT) representation, the power of the signal is within a small frequency range centered at the frequency f_0 of the sinusoidal signal that is applied to the speaker and all the other power is composed of noise and distortion. Figure 5.2(a) illustrates an example of FFT evaluation from the MI method, the green line indicate the FFT signal centered at the applied frequency (in this

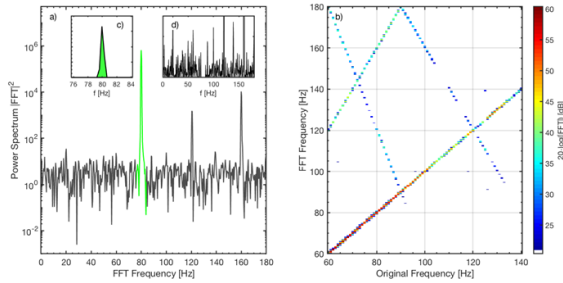


Figure 5.2 (a) Evaluation of the Signal-to-Noise and Distortion ratio (SINAD) from the Fast Fourier Transform (FFT) of the recovered signal from the MI method. (b) Spectrogram obtained with the Mean Intensity method.

case is $f_0 = 80$ Hz).

In addition to a peak at f_0 , peaks at other frequencies occur due to harmonics and aliasing. Figure 5.2(b) illustrates the appearance of other peaks, whose contribution is included in the noise and distortion term.

5.4 Results

The performance of the recovery methods are evaluated, firstly, when a sinusoidal signal was applied to the speaker. The performance comparison among the new algorithms and the others presented in the literature, is shown in Figure 5.3

The algorithms performances when a song is played by the speaker are measured by the Pearson coefficient. The comparison results for

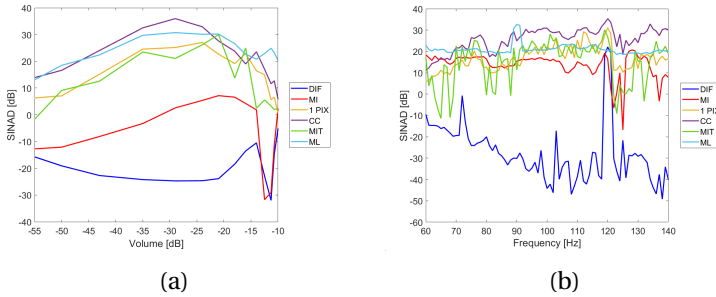


Figure 5.3 Methods performance comparison. (a) SINAD for increasing volume signal when the frequency is kept constant (100 Hz). (b) SINAD for increasing signal frequency when the signal volume is kept constant (-30dB, dB refers to sound pressure levels).

three different volumes and their mean execution time are shown in Table 5.1.

Combining the results shown in Figure 5.3 and Table 5.1, it is possible to note that, generally, the performance depends on the signal’s features. Nevertheless, comparing the execution time, it is possible to

Table 5.1 Performance of the song recovery for three volume levels and mean execution time.

	1 PIX	DIF	MI	MIT	ML	CC
-39.9 dB	0.4198	0.0415	0.2079	0.4321	0.4282	0.4308
-26.6 dB	0.3566	0.0591	0.1691	0.3032	0.4313	0.3540
-19.7 dB	0.1392	0.0601	0.0982	0.3084	0.7942	0.0972
Mean Time [s]	0.156	0.024	0.207	5.789	54.23	0.206

affirm that CC methods and 1 PIX give the best compromise between good performance and low computational cost.

5.5 Conclusion

An optical technique for remote sound recovering that allows to make non-contact vibration measurements is presented. Six different algorithms of remote recovery of audio signal were analysed. The comparison was performed in terms of quality of the recovered signals and computational costs. The best trade-off between performance and computational cost is the Cross-Correlation method. The technique under study can be implemented using a cheap setup composed by a low cost CCD camera and a low cost diode laser. The techniques analysed can be a basis for future applications in fusion imaging diagnostics to infer direct plasma measurements from indirect measurements. An example of application can be the measurement of fluctuations in fusion plasmas, using a similar procedure as performed in [88], in which the fluctuations measurement are performed using a phase contrast on tokamaks. The nuclear fusion field is open to innovation and the techniques presented pave the way for future plasma applications.

Chapter 6

Overall Conclusions and Future Perspectives

In this work, a contribution for the identification and control of non-linear phenomena, occurring during nuclear fusion experiments, was performed. Understanding the main rules that govern instability plasma phenomena is the key for tokamak operation safety, specifically during disruption. Different approaches and techniques were investigated.

In the first part of the thesis (Chapter 2), the design of an electrical analogue of a qualitative plasma behavioural model was presented. Results confirmed the potential of the circuit, able to mimic the physical behaviour of plasma quantities. The hybrid analogue model was designed and implemented in order to deeply investigate edge localized modes. Additionally, the analysis of the system dynamics before and after pellet injection and thermostat control was performed.

The results obtained allowed to confirm that the control strategies applied were able to mitigate the chaotic regime associated to the ELMs dynamics. The possibility to model complex phenomena using simple nonlinear electronic circuit is a powerful tool, allowing to test the dynamical behaviour of the system without running a real fusion experiment.

In Chapter 3 & 4 the analysis was focused on runaway electrons dynamics. Images of synchrotron radiation emission from RE were analysed and simulated in order to infer the RE parameters (pitch angle, energy). An automatic platform capable of inferring RE pitch angle from synchrotron spot was implemented. The results obtained were consistent with those in other tokamak machines. Furthermore, a detailed simulation of the images was carried out using the diagnostic tool SOFT. This code takes into account the geometric effects of the detected radiation and its radial distribution. The simulated images show a good matching with the experimental ones and the radiation spectra obtained in the experiments. Such studies, performed in parallel with the synchrotron spectra analysis, gave a better evaluation of the RE distribution function.

The last part of the thesis work (Chapter 5) presents a comparative study of different algorithms for the remote recovery of audio signal through the analysis of optical speckle patterns. Application of this technique can be envisaged, for example, for the measurement of fluctuations in fusion plasmas.

Investigation and control of plasma instabilities are important in view of the future operation of ITER, the largest experimental tokamak under construction in France. In this research context, it is

essential to increase the knowledge on complex and unstable phenomena affecting plasma stability. To reach this target it is necessary to develop accurate dynamical models and validate them matching with experiments. The work presented in this thesis represents a step forward plasma instabilities mitigation, obtained by both modelling plasma behaviour and test control strategies.

The research work performed has brought up interesting starting points for future research activities. The circuits implementation can be applied exploiting data of fusion experiments, allowing to perform a comparison with different machines and physical behaviours. The combined analysis of images and spectra has demonstrated to provide a better evaluation of RE parameters. In the future, the same type of analysis can be applied, systematically, to other discharges of the FTU database and other tokamak machines.

Bibliography

- [1] Thomas F Stocker, Dahe Qin, Gian-Kasper Plattner, Melinda Tignor, Simon K Allen, Judith Boschung, Alexander Nauels, Yu Xia, Vincent Bex, Pauline M Midgley, et al. *Climate change 2013: The physical science basis. Contribution of working group I to the fifth assessment report of the intergovernmental panel on climate change*, 1535, 2013.
- [2] Kenro Miyamoto. *Plasma physics for nuclear fusion*. MIT, 1980.
- [3] Jeffrey P Freidberg. *Plasma physics and fusion energy*. Cambridge university press, 2008.
- [4] John Wesson and David J Campbell. *Tokamaks*, volume 149. Oxford university press, 2011.
- [5] Allen H Boozer. Physics of magnetically confined plasmas. *Reviews of modern physics*, 76(4):1071, 2005.
- [6] James J Duderstadt and Gregory A Moses. *Inertial confinement fusion*. John Wiley & Sons, 1982.
- [7] ITER website. [online] <https://www.iter.org/>.
- [8] VP Smirnov. Tokamak foundation in ussr/russia 1950–1990. *Nuclear fusion*, 50(1):014003, 2009.
- [9] D Constantinescu, O Dumbrajs, V Igochine, K Lackner, R Meyer-Spasche, HAUT Zohm, and ASDEX Upgrade Team. A low-

- dimensional model system for quasi-periodic plasma perturbations. *Physics of Plasmas*, 18(6):062307, 2011.
- [10] FC Schuller. Disruptions in tokamaks. *Plasma Physics and Controlled Fusion*, 37(11A):A135, 1995.
- [11] Allen H Boozer. Theory of tokamak disruptions. *Physics of plasmas*, 19(5):058101, 2012.
- [12] Per Helander and Dieter J Sigmar. *Collisional transport in magnetized plasmas*, volume 4. Cambridge university press, 2005.
- [13] Enea website. [online] https://www.enea.it/it/Ricerca_sviluppo/nucleare/fusione-nucleare.
- [14] Ian H Hutchinson. Principles of plasma diagnostics. *Plasma Physics and Controlled Fusion*, 44(12):2603, 2002.
- [15] O Tudisco, GM Apruzzese, P Buratti, L Cantarini, A Canton, L Carraro, V Cocilovo, R de Angelis, M de Benedetti, B Esposito, et al. Chapter 8: The diagnostic systems in the ftu. *Fusion science and technology*, 45(3):402–421, 2004.
- [16] F Causa, M Gospodarczyk, P Buratti, D Carnevale, R De Angelis, B Esposito, A Grosso, G Maddaluno, José Ramón Martín-Solis, V Piergotti, et al. Runaway electron imaging spectrometry (REIS) system. *Review of Scientific Instruments*, 90(7):073501, 2019.
- [17] KH Finken, JG Watkins, D Rusbüldt, WJ Corbett, KH Dippel, DM Goebel, and RA Moyer. Observation of infrared synchrotron radiation from tokamak runaway electrons in textor. *Nuclear Fusion*, 30(5):859, 1990.
- [18] Jose Ramon Martin-Solis, Raul Sánchez, and Basilio Esposito. Experimental observation of increased threshold electric field for runaway generation due to synchrotron radiation losses in the ftu tokamak. *Physical review letters*, 105(18):185002, 2010.

-
- [19] A Stahl, O Embréus, G Papp, M Landreman, and T Fülöp. Kinetic modelling of runaway electrons in dynamic scenarios. *Nuclear Fusion*, 56(11):112009, 2016.
- [20] Mathias Hoppe. *Simulation and analysis of radiation from runaway electrons*. PhD thesis, Chalmers University of Technology, 2019.
- [21] Sundarapandian Vaidyanathan, Christos Volos, et al. *Advances and applications in nonlinear control systems*. Springer, 2016.
- [22] Arturo Buscarino, Luigi Fortuna, and Mattia Frasca. *Essentials of Nonlinear Circuit Dynamics with MATLAB® and Laboratory Experiments*. CRC Press, 2017.
- [23] Christopher Edwards and Sarah Spurgeon. *Sliding mode control: theory and applications*. Crc Press, 1998.
- [24] Randy Freeman and Petar V Kokotovic. *Robust nonlinear control design: state-space and Lyapunov techniques*. Springer Science & Business Media, 2008.
- [25] Concetta Barcellona. A new nonlinear circuit to identify plasma instabilities. *International Journal of Engineering Research and Technology*. ERSA Publication, 2278-0181, 2017.
- [26] Madhurjya P Bora and Dipak Sarmah. Sawtooth disruptions and limit cycle oscillations. *Communications in Nonlinear Science and Numerical Simulation*, 13(2):296–313, 2008.
- [27] Concetta Barcellona, Arturo Buscarino, Claudia Corradino, and Luigi Fortuna. Hybrid circuits to model and control fusion plasma instabilities. *IFAC-PapersOnLine*, 51(33):27–31, 2018.
- [28] Arturo Buscarino, Luigi Fortuna, Mattia Frasca, Gregorio Sciuto, et al. *A concise guide to chaotic electronic circuits*. Springer, 2014.

- [29] Todd E Evans, Richard A Moyer, Keith H Burrell, Max E Fenstermacher, Ilon Joseph, Anthony W Leonard, Thomas H Osborne, Gary D Porter, Michael J Schaffer, Philip B Snyder, et al. Edge stability and transport control with resonant magnetic perturbations in collisionless tokamak plasmas. *nature physics*, 2(6):419–423, 2006.
- [30] D Constantinescu, O Dumbrajs, V Igochine, K Lackner, H Zohm, ASDEX Upgrade Team, et al. Bifurcations and fast-slow dynamics in a low dimensional model for quasi-periodic plasma perturbations. *Romanian Reports in Physics*, 67(3):1049–1060, 2015.
- [31] Alan Wolf, Jack B Swift, Harry L Swinney, and John A Vastano. Determining lyapunov exponents from a time series. *Physica D: Nonlinear Phenomena*, 16(3):285–317, 1985.
- [32] Arduino board. [online] <http://www.arduino.cc/>.
- [33] D Constantinescu, O Dumbrajs, V Igochine, K Lackner, H Zohm, and ASDEX Upgrade Team. Rmp elm suppression analysis by means of a low-dimensional model system for quasi-periodic plasma perturbations. In *40th EPS Conference on Plasma Physics. European Physical Society*, 2013.
- [34] Shūichi Nosé. A molecular dynamics method for simulations in the canonical ensemble. *Molecular physics*, 52(2):255–268, 1984.
- [35] William G Hoover. Canonical dynamics: Equilibrium phase-space distributions. *Physical review A*, 31(3):1695, 1985.
- [36] Julien Clinton Sprott and William Graham Hoover. Harmonic oscillators with nonlinear damping. *International Journal of Bifurcation and Chaos*, 27(11):1730037, 2017.
- [37] Arturo Buscarino, Luigi Fortuna, and Mattia Frasca. The jerk dynamics of chua’s circuit. *International Journal of Bifurcation and Chaos*, 24(06):1450085, 2014.

-
- [38] HPW Gottlieb. Question# 38. what is the simplest jerk function that gives chaos? *AmJPh*, 64(5):525–525, 1996.
- [39] J C Sprott. A new class of chaotic circuit. *Physics Letters A*, 266(1):19–23, 2000.
- [40] Julien C Sprott. Simple chaotic systems and circuits. *American Journal of Physics*, 68(8):758–763, 2000.
- [41] Julien C Sprott. *Elegant chaos: algebraically simple chaotic flows*. World Scientific, 2010.
- [42] Julien Clinton Sprott. A new chaotic jerk circuit. *IEEE Transactions on Circuits and Systems II: Express Briefs*, 58(4):240–243, 2011.
- [43] Luigi Fortuna and Mattia Frasca. *Optimal and Robust Control: Advanced Topics with MATLAB®*. CRC press, 2012.
- [44] Nikolai G Lehtinen, Timothy F Bell, and Umran S Inan. Monte carlo simulation of runaway mev electron breakdown with application to red sprites and terrestrial gamma ray flashes. *Journal of Geophysical Research: Space Physics*, 104(A11):24699–24712, 1999.
- [45] Joseph R Dwyer. Relativistic breakdown in planetary atmospheres. *Physics of plasmas*, 14(4):042901, 2007.
- [46] Gordon D Holman. Acceleration of runaway electrons and joule heating in solar flares. In *Symposium-International Astronomical Union*, volume 107, pages 191–196. Cambridge University Press, 1985.
- [47] P Helander, LG Eriksson, and F Andersson. Runaway acceleration during magnetic reconnection in tokamaks. *Plasma Physics and Controlled Fusion*, 44(12B):B247, 2002.
- [48] Concetta Barcellona, Arturo Buscarino, Claudia Corradino, Luigi Fortuna, Federica Causa, Basilio Esposito, Giuseppe Mazzitelli, Giuliano Rocchi, Valerio Piergotti, Alessandro Sibio, et al.

- A procedure to estimate pitch angle for runaway electrons control in fusion reactors. In *2019 18th European Control Conference (ECC)*, pages 1159–1163. IEEE, 2019.
- [49] C. Barcellona, M. Bucolo, G. Stella, A. Buscarino, L. Fortuna, G. Mazzitelli, and B. Esposito. Advanced image-processing for the estimation of pitch angle for runaway electrons in tokamaks. In *2020 IEEE 20th Mediterranean Electrotechnical Conference (MELECON)*, pages 611–616, 2020.
- [50] JA Wesson, RD Gill, M Hugon, FC Schüller, JA Snipes, DJ Ward, DV Bartlett, DJ Campbell, PA Duperrex, AW Edwards, et al. Disruptions in jet. *Nuclear Fusion*, 29(4):641, 1989.
- [51] PC De Vries, MF Johnson, B Alper, P Buratti, TC Hender, HR Koslowski, V Riccardo, JET-EFDA Contributors, et al. Survey of disruption causes at jet. *Nuclear Fusion*, 51(5):053018, 2011.
- [52] Charles Thomson R Wilson. The electric field of a thundercloud and some of its effects. *Proceedings of the Physical Society of London*, 37(1):32D, 1924.
- [53] H Dreicer. Electron and ion runaway in a fully ionized gas. i. *Physical Review*, 115(2):238, 1959.
- [54] H Dreicer. Electron and ion runaway in a fully ionized gas. ii. *Physical review*, 117(2):329, 1960.
- [55] JW Connor and RJ Hastie. Relativistic limitations on runaway electrons. *Nuclear fusion*, 15(3):415, 1975.
- [56] Ola Embréus, Adam Stahl, and Tünde Fülöp. On the relativistic large-angle electron collision operator for runaway avalanches in plasmas. *Journal of Plasma Physics*, 84(1), 2018.
- [57] IUA Sokolov. Multiplication' of accelerated electrons in a tokamak. *JETP Letters*, 29:218–221, 1979.

- [58] MN Rosenbluth and SV Putvinski. Theory for avalanche of runaway electrons in tokamaks. *Nuclear Fusion*, 37(10):1355, 1997.
- [59] R Jayakumar, HH Fleischmann, and SJ Zweben. Collisional avalanche exponentiation of runaway electrons in electrified plasmas. *Physics Letters A*, 172(6):447–451, 1993.
- [60] Håkan Smith, P Helander, L-G Eriksson, and Tünde Fülöp. Runaway electron generation in a cooling plasma. *Physics of plasmas*, 12(12):122505, 2005.
- [61] Hakan M Smith and Erwin Verwichte. Hot tail runaway electron generation in tokamak disruptions. *Physics of Plasmas*, 15(7):072502, 2008.
- [62] F Andersson, P Helander, and L-G Eriksson. Damping of relativistic electron beams by synchrotron radiation. *Physics of Plasmas*, 8(12):5221–5229, 2001.
- [63] E Hirvijoki, I Pusztai, J Decker, O Embréus, A Stahl, and T Fülöp. Radiation reaction induced non-monotonic features in runaway electron distributions. *Journal of Plasma Physics*, 81(5), 2015.
- [64] B Esposito, L Boncagni, P Buratti, D Carnevale, F Causa, M Gospodarczyk, José Ramón Martín-Solis, Zana Popovic, M Agostini, G Apruzzese, et al. Runaway electron generation and control. *Plasma Physics and Controlled Fusion*, 59(1):014044, 2016.
- [65] Wolfgang Rindler. *Relativity: special, general, and cosmological*, 2003.
- [66] Mateusz Gospodarczik. *Control, diagnostics and estimation techniques for runaway electrons beams*. PhD thesis, Università degli studi di Roma "Tor Vergata", 2018.
- [67] JH Yu, EM Hollmann, N Commaux, NW Eidietis, DA Humphreys, AN James, Thomas C Jernigan, and RA Moyer. Visible imaging

- and spectroscopy of disruption runaway electrons in DIII-D. *Physics of Plasmas*, 20(4):042113, 2013.
- [68] R.J.E Jaspers. *Relativistic runaway electrons in tokamak plasmas*. PhD thesis, Technische Universiteit Eindhoven, 1995.
- [69] R Jaspers, NJ Lopes Cardozo, AJH Donne, HLM Widdershoven, and KH Finken. A synchrotron radiation diagnostic to observe relativistic runaway electrons in a tokamak plasma. *Review of Scientific Instruments*, 72(1):466–470, 2001.
- [70] I Entrop, R Jaspers, NJ Lopes Cardozo, and KH Finken. Runaway snakes in textor-94. *Plasma physics and controlled fusion*, 41(3):377, 1999.
- [71] IM Pankratov. Analysis of the synchrotron radiation emitted by runaway electrons. *Plasma Physics Reports*, 22(6):535, 1996.
- [72] D Del-Castillo-Negrete, G. Zhang, L. Cabajal, J. Lore, D. Spong, and S. Seal. Integrated simulation of runaway electrons: a backward monte-carlo approach for a fluid-kinetic self-consistent coupling. *IAEA*, 2018.
- [73] Mathias Hoppe, Ola Embréus, R Alexander Tinguely, Robert S Granetz, Adam Stahl, and Tünde Fülöp. Soft: a synthetic synchrotron diagnostic for runaway electrons. *Nuclear Fusion*, 58(2):026032, 2018.
- [74] Adam Stahl, Matt Landreman, Gergely Papp, Eric Hollmann, and Tünde Fülöp. Synchrotron radiation from a runaway electron distribution in tokamaks. *Physics of Plasmas*, 20(9):093302, 2013.
- [75] How to read ftu data from a remote connection. [online] https://lost-contact.mit.edu/afs/fusione.it/user/home/benedett/public/public_html/RemoteFtuData/index.htm.
- [76] Softv2’s documentation. [online] <https://soft2.readthedocs.io/en/latest/index.html>.

- [77] *CCD Micro Camera head 1/2" IK-M51H.*
- [78] Tünde Fülöp, Gergö Pokol, Per Helander, and Mietek Lisak. Destabilization of magnetosonic-whistler waves by a relativistic runaway beam. *Physics of Plasmas*, 13(6):062506, 2006.
- [79] Concetta Barcellona, Donatus Halpaap, Pablo Amil, Arturo Buscarino, Luigi Fortuna, Jordi Tiana-Alsina, and Cristina Masoller. Remote recovery of audio signals from videos of optical speckle patterns: a comparative study of signal recovery algorithms. *Optics express*, 28(6):8716–8723, 2020.
- [80] Joseph W Goodman. *Speckle phenomena in optics: theory and applications*. Roberts and Company Publishers, 2007.
- [81] Luis Rodriguez-Cobo, Mauro Lomer, and Jose-Miguel Lopez-Higuera. Fiber specklegram-multiplexed sensor. *Journal of Lightwave Technology*, 33(12):2591–2597, 2014.
- [82] Ignacio Robles-Urquijo, M Lomer, Luis Rodriguez-Cobo, and José Miguel Lopez-Higuera. Non-contact vibration analysis using speckle-based techniques. In *2017 25th Optical Fiber Sensors Conference (OFS)*, pages 1–4. IEEE, 2017.
- [83] Joshua B Tenenbaum, Vin De Silva, and John C Langford. A global geometric framework for nonlinear dimensionality reduction. *science*, 290(5500):2319–2323, 2000.
- [84] Abe Davis, Michael Rubinstein, Neal Wadhwa, Gautham J Mysore, Frédo Durand, and William T Freeman. The visual microphone: Passive recovery of sound from video. 2014.
- [85] Javier Portilla and Eero P Simoncelli. A parametric texture model based on joint statistics of complex wavelet coefficients. *International journal of computer vision*, 40(1):49–70, 2000.
- [86] Eero P Simoncelli, William T Freeman, Edward H Adelson, and David J Heeger. Shiftable multiscale transforms. *IEEE transactions on Information Theory*, 38(2):587–607, 1992.

- [87] Walt Kester. Understand sinad , enob , snr , thd , $\text{thd} + n$, and sfd so you don't get lost in the noise floor. *MT-003 Tutorial*, www.analog.com/static/importedfiles/tutorials/MT-003.pdf, 2009.
- [88] Henri Weisen. Optical diagnostics for plasma density fluctuations. Technical report, 1999.